

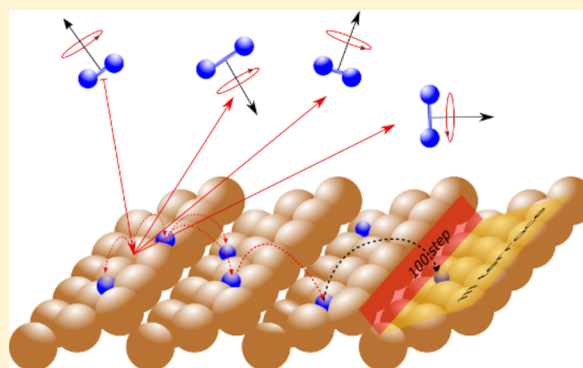
# Quantum Dynamics of Dissociative Chemisorption of H<sub>2</sub> on the Stepped Cu(211) Surface

Egidius W. F. Smeets,<sup>†</sup> Gernot Fuchsel,<sup>‡</sup> and Geert-Jan Kroes<sup>\*,†</sup>

<sup>†</sup>Leiden Institute of Chemistry, Gorlaeus Laboratories, Leiden University, P.O. Box 9502, 2300 RA Leiden, The Netherlands

<sup>‡</sup>Institut für Chemie und Biochemie - Physikalische und Theoretische Chemie, Freie Universität Berlin, Takustraße 3, 14195 Berlin, Germany

**ABSTRACT:** Reactions on stepped surfaces are relevant to heterogeneous catalysis, in which a reaction often takes place at the edges of nanoparticles where the edges resemble steps on single-crystal stepped surfaces. Previous results on H<sub>2</sub> + Cu(211) showed that, in this system, steps do not enhance the reactivity and raised the question of whether this effect could be, in any way, related to the neglect of quantum dynamical effects in the theory. To investigate this, we present full quantum dynamical molecular beam simulations of sticking of H<sub>2</sub> on Cu(211), in which all important rovibrational states populated in a molecular beam experiment are taken into account. We find that the reaction of H<sub>2</sub> with Cu(211) is very well described with quasi-classical dynamics when simulating molecular beam sticking experiments, in which averaging takes place over a large number of rovibrational states and over translational energy distributions. Our results show that the stepped Cu(211) surface is distinct from its component Cu(111) terraces and Cu(100) steps and cannot be described as a combination of its component parts with respect to the reaction dynamics when considering the orientational dependence. Specifically, we present evidence that, at translational energies close to the reaction threshold, vibrationally excited molecules show a negative rotational quadrupole alignment parameter on Cu(211), which is not found on Cu(111) and Cu(100). The effect arises because these molecules react with a site-specific reaction mechanism at the step, that is, inelastic rotational enhancement, which is only effective for molecules with a small absolute value of the magnetic rotation quantum number. From a comparison to recent associative desorption experiments as well as Born–Oppenheimer molecular dynamics calculations, it follows that the effects of surface atom motion and electron–hole pair excitation on the reactivity fall within chemical accuracy, that is, modeling these effect shifts extracted reaction probability curves by less than 1 kcal/mol translational energy. We found no evidence in our fully state-resolved calculations for the “slow” reaction channel that was recently reported for associative desorption of H<sub>2</sub> from Cu(111) and Cu(211), but our results for the fast channel are in good agreement with the experiments on H<sub>2</sub> + Cu(211).



## 1. INTRODUCTION

The rate-limiting step in heterogeneous catalysis is often a dissociative chemisorption reaction.<sup>1,2</sup> Hydrogen (H<sub>2</sub>) dissociation is important to the heterogeneously catalyzed production of syngas and ammonia<sup>3</sup> and has recently gained industrial importance with the production of methanol from CO<sub>2</sub> over a Cu/ZnO/Al<sub>2</sub>O<sub>3</sub> catalysts, in which the rate-limiting step is considered to be the dissociation of H<sub>2</sub>.<sup>4–6</sup> Stepped, kinked, or otherwise defective surfaces more closely resemble real catalytic surfaces, as catalyzed reactions tend to proceed at the corners or edges of nanoparticles.<sup>7,8</sup> A better theoretical understanding of the reaction dynamics of H<sub>2</sub> dissociation on stepped surfaces could well be a first step to the design of new catalysts from first principles.<sup>9</sup>

H<sub>2</sub> reacting on copper surfaces is a prototypical example of a highly activated late barrier system.<sup>10–13</sup> For the flat Cu(111), Cu(110), and Cu(100) surfaces, a plethora of experimental<sup>13–24</sup> and theoretical<sup>12,15–43</sup> results have been reported,

which are generally in good agreement with each other. This large body of work has allowed for the development of a chemically accurate description of molecular beam experiments using the semiempirical specific reaction parameter approach to density functional theory (SRP-DFT).<sup>35</sup> Recently, molecular beam adsorption experiments<sup>44</sup> and associative desorption experiments<sup>45</sup> for H<sub>2</sub> reacting on Cu(211) have been reported, allowing for a more stringent comparison between theory and experiment for this system that more closely resembles a catalytic particle. Theoretical reaction dynamics of H<sub>2</sub> reacting on stepped or defective surfaces have only been reported sparingly, most notably for D<sub>2</sub> on Cu(211),<sup>46</sup> H<sub>2</sub> on Pt(211),<sup>47–51</sup> and H<sub>2</sub> on defective Pd(111).<sup>52</sup>

Received: July 10, 2019

Revised: August 22, 2019

Published: August 23, 2019

In our previous work, we and others have shown that the Cu(211) surface is less reactive than the Cu(111) surface,<sup>46</sup> which indicates that predictions based on the d-band model of Nørskov and Hammer<sup>53,54</sup> are not always reliable. In the d-band model, increased reactivity at steps, defects, or otherwise less coordinated surface atoms is ascribed to a reduced width of the d band<sup>53,55</sup> and a shift of the center of the d band toward the Fermi level at these sites. In the case of Cu(211), the breakdown of the d-band model is due to the geometric effect of the lowest barrier to the reaction of H<sub>2</sub> on Cu(111) not being situated at a top site.<sup>46</sup>

Due to the corrugated nature of the molecule surface interaction and the denser distribution of barriers to the reaction, it is unclear whether quantum effects can have a significant effect on the reaction dynamics of H<sub>2</sub> reacting on Cu(211). Our main goal is to investigate if including quantum effects during the dynamics significantly affects observables such as the macroscopic molecular reaction probability and rotational quadrupole alignment parameters. To this end, we will mainly focus on a comparison of fully state-resolved quantum dynamical (QD) and quasi-classical trajectory (QCT) reaction probabilities for H<sub>2</sub> incident on Cu(211), and the effect of Boltzmann averaging over all rovibrational states populated in a molecular beam experiment. Employing the time-dependent wave packet (TDWP) method,<sup>56,57</sup> we have carried out QD calculations mainly for H<sub>2</sub>. Due to the low mass of H<sub>2</sub>, quantum effects are presumed to be most prevalent for H<sub>2</sub>, and energy transfer to the surface during collision is expected to be small. Performing this large body of calculations for D<sub>2</sub> would have been much more expensive because its larger mass necessitates the use of denser numerical grids and longer propagation times.

Another aim will be to investigate if the reaction dynamics of H<sub>2</sub> dissociation on the stepped Cu(211) differs from the reaction dynamics at low Miller index copper surfaces, for which the reaction dynamics is reasonably similar.<sup>30–32,43</sup> This is relevant because the Cu(211) surface has Cu(111) terraces and Cu(100) steps, and considering this question might thus provide more insight in how a stepped surface can alter reaction mechanisms. Rotational quadrupole alignment parameters for vibrationally excited molecules are similar in behavior for Cu(111)<sup>16,32</sup> and Cu(100).<sup>30,31</sup> We will investigate whether the same holds for H<sub>2</sub> + Cu(211).

Recent associative desorption experiments on Cu(111) and Cu(211),<sup>45</sup> which were in good agreement with earlier theoretical and experimental works,<sup>16,30,34,35,46,58</sup> have shown a never before reported “slow” reaction channel to be active for both Cu(111) and Cu(211). In this channel, the reaction could be facilitated by trapping on the surface and distortion of the surface due to thermal motion forming a reactive site.<sup>45</sup> Our calculations on sticking of H<sub>2</sub> are carried out using the static surface approximation, which suggest that we might not be able to model this slow channel. We do however make a direct comparison to the experimental effective barrier heights obtained by applying the principle of detailed balance and direct inversion of time-of-flight measurements reported by Kaufmann et al.<sup>45</sup> for the fast channel.

The highly accurate potential energy surface (PES) used in our calculations and our previous work<sup>46</sup> has been constructed using the corrugation reducing procedure (CRP)<sup>59</sup> together with the SRP48 SRP density functional,<sup>32</sup> which was proven to be chemically accurate for H<sub>2</sub> dissociating on Cu(111).<sup>35</sup> It has also been shown previously that the SRP functional for H<sub>2</sub> +

Cu(111) is transferable to H<sub>2</sub> + Cu(100).<sup>30</sup> All our calculations have been carried out using the BOSS model, which works well for activated H<sub>2</sub> dissociation on metals at low surface temperatures.<sup>26,33–36,60</sup>

This paper is organized as follows. Section 2 will outline the computational methods used, with Section 2.A detailing the coordinate system used and Section 2.B describing the AIMD calculations. Sections 2.C and 2.D describe the QCT and QD methods, respectively, while Section 2.E describes the calculations of observables. Section 3 is the results and discussion section. Section 3.A is a comparison between QD and QCT reaction probabilities at the fully state-resolved level. Section 3.B presents calculated rotational quadrupole alignment parameters for both H<sub>2</sub> and D<sub>2</sub>. In Section 3.C, we compare theory to the experimental effective barrier heights reported by Kaufmann et al.<sup>45</sup> Section 3.D presents a comparison of BOMD, QCT, and molecular dynamics with electronic friction (MDEF) calculations for D<sub>2</sub> in order to highlight the extent to which surface atom motion and electron–hole pair (ehp) excitation can be expected to affect the reaction probability in molecular beam experiments. In Section 3.E, we present fully quantum dynamical molecular beam simulations for H<sub>2</sub> reacting on Cu(211), comparing to QCT calculations. Section 4 presents conclusions.

## 2. COMPUTATIONAL METHODS AND SIMULATIONS

In the following, we present details about the different simulations we have performed to describe the dynamics of H<sub>2</sub>(D<sub>2</sub>) incident on Cu(211). In our six-dimensional QD, QCT, and MDEF simulations, we used the static surface approximation. They are carried out on a six-dimensional PES that was previously developed by us<sup>46</sup> on the basis of the corrugation reducing procedure<sup>49</sup> and ~116,000 DFT energy points computed with the SRP48 functional.<sup>32</sup> The SRP48 functional contains 48% RPBE<sup>61</sup> and 52% PBE<sup>62</sup> exchange correlation and was fitted to quantitatively reproduce experimental sticking probabilities for the reaction of H<sub>2</sub>(D<sub>2</sub>) on a flat Cu(111) surface.<sup>32</sup> The very similar SRP functional<sup>35</sup> performed well at describing the H<sub>2</sub> + Cu(100) reaction.<sup>30</sup>

**2.A. Coordinate System.** The six-dimensional dynamics calculations account only for the motion along the six molecular degrees of freedom (DOF) of H<sub>2</sub>(D<sub>2</sub>), while the surface atoms are kept frozen at their ideal 0 K configuration as computed with DFT. The molecular coordinates include the center of mass (COM) position given by the coordinates *X*, *Y*, and *Z*, where *Z* is the molecule–surface distance, and *X* and *Y* are the lateral positions measured relative to a Cu reference atom at the step edge. Also included are the H–H bond distance *r* and the angular orientation of H<sub>2</sub> given by the polar angle *θ* defined with respect to the surface normal and the azimuthal angle *φ*. The coordinate system is drawn in Figure 1a, and the Cu(211) surface unit cell is drawn in Figure 1b; additional details about the dimensions of the (1 × 1)Cu(211) unit cell are specified in the corresponding caption.

**2.B. Ab Initio Molecular Dynamics Simulations.** To describe the reaction of D<sub>2</sub> on Cu(211) at normal incidence with the BOMD technique, we employ a modified version of the Vienna ab initio simulation package<sup>63–66</sup> (VASP). Note that, in previous publications, we referred to the direct dynamics technique using SRP-DFT as the ab initio molecular dynamics (AIMD) method. Because this might be taken to imply that the SRP functional is not semiempirical, we abandoned this name and now refer to it as Born–

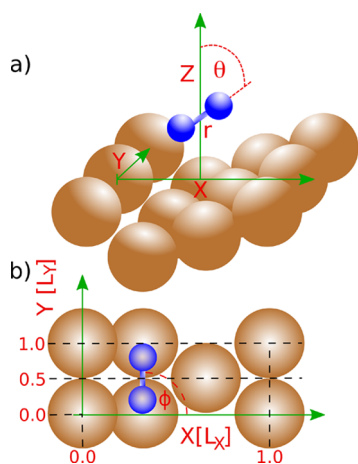


**Figure 1.** Coordinate system for  $\text{H}_2(\text{D}_2)$  on  $\text{Cu}(211)$ . H atoms are drawn in blue, and Cu atoms are drawn in brown. Shown are (a) a side view on a  $(1 \times 2)\text{Cu}(211)$  supercell and (b) a top view on a  $(1 \times 1)$  unit cell. The six-dynamical molecular DOF are indicated, that is, the COM coordinates given by  $X$ ,  $Y$ , and  $Z$ , where  $X$  and  $Y$  are the lateral coordinates and  $Z$  is the molecule surface distance. Further, the H–H bond distance is represented by  $r$ , and the angular orientation is represented by the polar angle  $\theta$  and the azimuthal angle  $\phi$ . The latter is defined with respect to the  $X$  axis, and the former is defined with respect to the macroscopic surface normal. The computed lengths of the lattice vectors of the  $(1 \times 1)$  unit cell are  $L_X = 6.373 \text{ \AA}$  and  $L_Y = 2.602 \text{ \AA}$  along  $X$  and  $Y$ .

Oppenheimer molecular dynamics (BOMD). The modifications of the computer package concern the propagation algorithm and were first introduced in previous works<sup>67,68</sup> on electronically nonadiabatic effects in gas–surface systems using VASP. To be consistent with our previous work on the system,<sup>46</sup> we adopt the same computational setup for the electronic structure calculations specified in the Supporting Information of ref 46. Here, we briefly recall only the most important details. The  $\text{Cu}(211)$  surface is represented using a five-layer slab model periodically repeated over a  $(1 \times 2)$  supercell with a vacuum spacing of  $15 \text{ \AA}$ . Ultrasoft pseudopotentials are used as well as plane waves corresponding to energies of up to  $370 \text{ eV}$ . The  $k$ -points are sampled using the Monkhorst grid scheme and an  $8 \times 8 \times 1$  mesh centered at the  $\Gamma$  point. Fermi smearing is used with a width of  $0.1 \text{ eV}$ .

BOMD simulations are performed at different average incidence energies and mimic corresponding molecular beam conditions at which Michelsen et al.<sup>15</sup> originally performed experiments on the dissociation of  $\text{D}_2$  on flat  $\text{Cu}(111)$ . The inclusion of beam parameters in the simulations is explained below in Section 2.E. For each incidence energy point, we perform 500 trajectory calculations. This allows us to achieve an absolute standard error of smaller than  $0.02$  in the computed initial sticking coefficient. All BOMD trajectories start at a molecule–surface distance of  $Z = 7 \text{ \AA}$  and are propagated until dissociation or scattering of  $\text{D}_2$  has occurred. Here, we count trajectories to be dissociatively adsorbed if the D–D bond distance  $r$  is larger than  $2.45 \text{ \AA}$ . A nonreactive scattering event is counted when trajectories return to the gas phase and have reached a molecule–surface distance of  $Z \geq 7.1 \text{ \AA}$ . We use a time-step discretization  $\Delta t$  of  $1 \text{ fs}$  in the dynamics propagation and a maximum propagation time  $t_f$  of  $2 \text{ ps}$ . Geometries between consecutive time steps are updated if the electronic structure energy is converged to  $10^{-5} \text{ eV}$ . The

setup allows, on average, for an energy conservation error of typically  $\sim 10 \text{ meV}$ .

BOMD simulations performed within the static surface approximation employ the same slab model described in our earlier work.<sup>46</sup> Therein, the first four layers of the slab are relaxed through energy minimization (the positions of the fifth layer atoms are fixed during relaxation). The resulting optimized  $\text{Cu}(211)$  surface conserves the  $P1m1$  space group and remains unchanged during the BOMD simulations. This prevents energy transfer to take place between the molecule and the surface due to excitation of surface atom motion upon scattering. To model a thermalized  $\text{Cu}(211)$  surface at a temperature  $T_s$  of  $120 \text{ K}$  according to experiments, we follow the NVE/NVT procedure explained in refs 32. and 69 and generate 10,000 slab configurations resembling the phase space. The initial condition of a BOMD trajectory at  $T_s = 120 \text{ K}$  is set up by randomly mixing thermalized slab models with random configurations of  $\text{D}_2$  generated according to the molecular beam conditions.

**2.C. Quasi-Classical Simulations.** The MD(EF) simulations presented in this work use the 6D PES of ref 46 and assume quasi-classical conditions,<sup>70</sup> that is, initial conditions of the classical trajectories reflect the quantum mechanical energies of incident  $\text{H}_2$  ( $\text{D}_2$ ) in their initial rovibrational state(s). To do so, we use the method described in ref 69. The dynamics is studied by integrating a Langevin equation<sup>71</sup> numerically using the stochastic Ermak–Buckholz algorithm,<sup>72</sup> and the methodology is outlined in refs 69 and 73. Note that, in the nondissipative limit, that is, the MD case, the Langevin equation obeys Newton’s equation of motion for which the propagation algorithm is also suitable. In the MDEF case, energy dissipation between the molecule and surface is mediated through electronic friction as computed from the local density friction approximation within the independent atom approximation (LDFA-IAA) model.<sup>74</sup> Specifically, friction coefficients of the hydrogen atoms are represented as a function of the electron density of the ideal bare  $\text{Cu}(211)$  surface. The latter is extracted from a single DFT calculation (see ref 69 for details).

QCT calculations are used here (i) to model fictitious molecular beam experiments using realistic beam parameters and (ii) to perform initial state-resolved calculations. In the former case, 100,000 QCT calculations per energy point are computed, whereas state-resolved sticking coefficients are evaluated per energy point over 50,000 trajectories. As with BOMD, all MD(EF) trajectories start at a molecule–surface distance of  $Z = 7 \text{ \AA}$ . A time step of  $\Delta t = 0.5 \hbar/E_h$  ( $\approx 0.012 \text{ fs}$ ) is used for the propagation resulting in an energy conservation error for the MD simulations of smaller than  $1 \text{ meV}$ . To determine dissociative adsorption and nonreactive scattering, we impose the same conditions used for the BOMD simulations (see above).

**2.D. Quantum Dynamics Simulations.** To perform 6D quantum dynamics simulations, we solve the time-dependent Schrödinger equation

$$i\hbar \frac{d\Psi(\underline{Q}; t)}{dt} = \hat{H}(\underline{Q})\Psi(\underline{Q}; t) \quad (1)$$

using the time-dependent wave packet (TDWP) approach as implemented in our in-house computer package.<sup>56,57</sup> In eq 1,  $\underline{Q} = (X, Y, Z, r, \theta, \phi)^T$  is a six-dimensional position vector,  $\Psi(\underline{Q}; t)$  is the time-dependent nuclear wave function of the system, and  $\hat{H}(\underline{Q})$  is the time-independent Hamiltonian, which reads

Table 1. Input Parameters for the 6D Quantum Simulations on the Reactive Scattering of H<sub>2</sub> on Cu(211)<sup>a</sup>

| parameters                                     | 0.05–0.22 eV |         | 0.2–0.6 eV |         | 0.57–1.4 eV          |                       | D <sub>2</sub> |             |
|--|--------------|---------|------------|---------|----------------------|-----------------------|----------------|-------------|
|  | $\nu_0$      | $\nu_1$ | $\nu_0$    | $\nu_1$ | $\nu_0 J \in [0, 7]$ | $\nu_0 J \in [8, 11]$ | $\nu_1$        | $\nu_1 J_6$ |
| $Z_{\text{start}}$ (bohr)                      | –2.0         | –2.0    | –2.0       | –2.0    | –2.0                 | –2.0                  | –2.0           | –2.0        |
| $N_{Z_{\text{spec}}}$                          | 280          | 280     | 280        | 280     | 280                  | 280                   | 280            | 280         |
| $N_Z$  | 180          | 180     | 176        | 176     | 176                  | 176                   | 176            | 176         |
| $\Delta Z$ (bohr)                              | 0.1          | 0.1     | 0.08       | 0.08    | 0.08                 | 0.08                  | 0.08           | 0.08        |
| $R_{\text{start}}$ (bohr)                      | 0.8          | 0.8     | 0.8        | 0.8     | 0.8                  | 0.8                   | 0.8            | 0.8         |
| $N_R$  | 60           | 60      | 56         | 56      | 56                   | 56                    | 56             | 56          |
| $\Delta R$ (bohr)                              | 0.15         | 0.15    | 0.15       | 0.15    | 0.15                 | 0.15                  | 0.15           | 0.15        |
| $N_X$  | 36           | 36      | 36         | 36      | 36                   | 36                    | 36             | 42          |
| $N_Y$  | 12           | 12      | 12         | 12      | 12                   | 12                    | 12             | 16          |
| $N_J$  | 26 / 25      | 30 / 29 | 26 / 25    | 32 / 31 | 38 / 37              | 42 / 41               | 36 / 35        | 42          |
| $N_{m_j}$                                      | 26 / 25      | 30 / 29 | 26 / 25    | 32 / 31 | 30 / 29              | 42 / 41               | 28 / 27        | 40          |
| Complex absorbing potentials                   |              |         |            |         |                      |                       |                |             |
| $Z^{\text{CAP}}$ start ( $a_0$ )               | 8.9          | 8.9     | 8.88       | 8.88    | 8.88                 | 8.88                  | 8.88           | 8.88        |
| $Z^{\text{CAP}}$ end ( $a_0$ )                 | 15.9         | 15.9    | 12.0       | 12.0    | 12.0                 | 12.0                  | 12.0           | 12.0        |
| $Z^{\text{CAP}}$ optimum (eV)                  | 0.16         | 0.16    | 0.3        | 0.3     | 0.95                 | 0.95                  | 0.95           | 0.3         |
| $Z_{\text{spec}}^{\text{CAP}}$ start ( $a_0$ ) | 18.1         | 18.1    | 16.8       | 16.8    | 18.16                | 18.16                 | 18.16          | 16.8        |
| $Z_{\text{spec}}^{\text{CAP}}$ end ( $a_0$ )   | 25.9         | 25.9    | 20.32      | 20.32   | 20.32                | 20.32                 | 20.32          | 20.32       |
| $Z_{\text{spec}}^{\text{CAP}}$ optimum (eV)    | 0.16         | 0.16    | 0.3        | 0.3     | 1.2                  | 1.2                   | 1.2            | 0.3         |
| $R^{\text{CAP}}$ start ( $a_0$ )               | 4.55         | 4.55    | 4.55       | 4.55    | 4.55                 | 4.55                  | 4.55           | 4.55        |
| $R^{\text{CAP}}$ end ( $a_0$ )                 | 9.65         | 9.65    | 9.05       | 9.05    | 9.05                 | 9.05                  | 9.05           | 9.05        |
| $R^{\text{CAP}}$ optimum (eV)                  | 0.12         | 0.12    | 0.3        | 0.3     | 1.0                  | 1.0                   | 1.0            | 0.3         |
| Propagation                                    |              |         |            |         |                      |                       |                |             |
| $\Delta t$ ( $\hbar/E_h$ )                     | 2            | 2       | 2          | 2       | 2                    | 2                     | 2              | 2           |
| $t_f$ ( $\hbar/E_h$ )                          | 44000        | 44000   | 14000      | 14000   | 10000                | 10000                 | 10000          | 20000       |
| Initial wave packet                            |              |         |            |         |                      |                       |                |             |
| $E_{\text{min}}$ (eV)                          | 0.05         | 0.05    | 0.2        | 0.2     | 0.57                 | 0.57                  | 0.57           | 0.2         |
| $E_{\text{max}}$ (eV)                          | 0.22         | 0.22    | 0.6        | 0.6     | 1.4                  | 1.4                   | 1.4            | 0.6         |
| $Z_0$ ( $a_0$ )                                | 13.50        | 13.5    | 11.44      | 11.44   | 11.44                | 11.44                 | 11.44          | 11.44       |

<sup>a</sup>All wave packets were propagated until the remaining norm was less than 1%.

$$\hat{H}(\underline{Q}) = -\frac{\hbar^2}{2M}\nabla^2 - \frac{\hbar^2}{2\mu}\frac{\partial^2}{\partial r^2} + \frac{1}{2\mu r^2}\hat{J}^2(\theta, \phi) + V(\underline{Q}) \quad (2)$$

Here,  $M$  and  $\mu$  are the mass and the reduced mass of H<sub>2</sub>, respectively, and  $\nabla$  and  $\hat{J}$  are the nabla and the angular momentum operators. The 6D PES,  $V(\underline{Q})=V(X,Y,Z,r,\theta,\phi)$ , is taken from ref 46 and was computed with the SRP48 functional.<sup>32</sup> The initial wave function is represented as a product of a Gaussian wave packet  $u(Z_0, k_0^Z)$  centered around  $Z_0$ , a two-dimensional plane wave function  $\phi(k_0^X, k_0^Y)$  along  $X$  and  $Y$ , and the rovibrational wave function  $\psi_{\nu, j, m_j}(r, \theta, \phi)$  of incident H<sub>2</sub>

$$\Psi(\underline{Q}, t = 0) = \psi_{\nu, j, m_j}(r, \theta, \phi)\phi(k_0^X, k_0^Y)u(Z; Z_0, k_0^Z) \quad (3)$$

where the two-dimensional plain wave function and the Gaussian wave packet are defined as

$$\phi(k_0^X, k_0^Y) = e^{i(k_0^X X_0 + k_0^Y Y_0)} \quad (4)$$

$$u(Z; Z_0, k_0^Z) = \left(\frac{2\sigma^2}{\pi}\right)^{1/4} \int_0^\infty dk_0^Z e^{-\sigma^2(\underline{k}-k_0^Z)} e^{i(\underline{k}-k_0^Z)Z_0} e^{ik_0^Z Z_0} \quad (5)$$

Here,  $\sigma$  is the width of the wave packet centered around the wave vector  $\underline{k}$ , and  $k_0^{X,Y,Z}$  are the initial wave vectors of the

COM. The width  $\sigma$  is chosen in such a way that 90% of the Gaussian wave packet is placed in an energy range  $E_i \in [E_{\text{min}}, E_{\text{max}}]$ . Equation 1 is solved numerically using the split operator method with a time step  $\Delta t$ . We apply a quadratic form of optical potentials<sup>75</sup> in the scattering (large values of  $Z$ ) and adsorption regions (large values of  $r$ ). The scattered fraction of the wave function is analyzed through the scattering matrix formalism,<sup>76</sup> and the scattering probability  $P_{\text{sc}}$  is computed accordingly. Subtracting  $P_{\text{sc}}$  from 1 then yields the sticking probability  $S_0$ .

Parameters for the wave packet calculations defining the initial wave packet, grid representation, time step, and the optical potentials are compiled in Table 1. The final propagation time can vary since we stop simulations if the remaining norm on the grid is below 0.01.

**2.E. Computation of Observables.** To incorporate the effect of a molecular beam on the computed sticking coefficient, we need to take into account the distributions of translational energies and rovibrational state population due to a nozzle temperature  $T_n$ . The probability to find a molecule with velocity  $v + dv$  and a rovibrational state described by the vibrational quantum number  $\nu$  and the angular momentum quantum number  $j$  here is given by

$$P(\nu, \nu, J, T_n)dv = P_{\text{flux}}(\nu; T_n)dv \times P_{\text{int}}(\nu, J, T_n) \quad (6)$$

where the flux-weighted velocity distribution  $P_{\text{flux}}$  is a parameterized function of  $T_n$  and determined by the width parameter  $\alpha$  and the stream velocity  $v_0$  according to<sup>77</sup>

$$P_{\text{flux}}(\nu; T_n) d\nu = C\nu^3 e^{-(\nu-\nu_0)^2/\alpha^2} d\nu \quad (7)$$

where  $C$  is a normalization constant. The ensemble representation of the rovibrational state population distribution reads

$$P_{\text{int}}(\nu, J, T_n) = \frac{w(J)f(\nu, J, T_n)}{\sum_{\nu', J' \equiv J \pmod{2}} f(\nu', J', T_n)} \quad (8)$$

with

$$f(\nu, J, T_n) = (2J + 1) \times e^{-(E_{\nu,0} - E_{0,0})/k_B T_{\text{vib}}} \times e^{-(E_{\nu,J} - E_{\nu,0})/k_B T_{\text{rot}}} \quad (9)$$

Here,  $k_B$  is the Boltzmann constant, and  $E_{\nu,j}$  is the energy of the quantum state characterized by  $\nu$  and  $j$ . The first and second Boltzmann factors describe the vibrational and rotational state populations, respectively. Note that the rotational temperature is  $T_{\text{rot}} = 0.8T_n$ ,<sup>18</sup> whereas the vibrational temperature applies  $T_{\text{vib}} = T_n$ . This setting is in agreement with the observation that rotational but no vibrational cooling occurs during gas expansion in the nozzle. The factor  $w(J)$  in eq 8 is due to *ortho*- and *para*-hydrogen molecules present in the beam. For  $\text{H}_2$ ,  $w(J)$  is 1/4 (3/4) for even (odd) values of  $J$ , and for  $\text{D}_2$ ,  $w(J) = 2/3$  (1/3) for even (odd) values of  $J$ .

In the case of classical dynamics calculations (MD, MDEF, and BOMD), the probability distributions  $P(\nu, \nu, J, T_n)$  is randomly sampled as described in ref 69 using the different beam parameters on  $\text{H}_2$  and  $\text{D}_2$  listed in Table 2. The sticking coefficient per energy point is given by the ratio of the number of adsorbed trajectories  $N_{\text{ads}}$  and the total number of computed trajectories  $N$ , that is,  $S_0 = N_{\text{ads}}/N$ . To extract quantum mechanical results on  $\text{H}_2$  beam simulations, a direct sampling of  $P(\nu, \nu, J, T_n)$  is not feasible. Instead, initial state-resolved reaction probabilities  $R_{\text{mono}}(E_i, \nu, J)$  are first computed as functions of the monochromatic incidence energy  $E_i$  by degeneracy averaging fully initial state-resolved reaction probabilities  $P_{\text{R}}(E_i, \nu, J, m_j)$  over the magnetic rotational quantum number  $m_j$ , that is,

$$R_{\text{mono}}(E_i, \nu, J) = \frac{\sum_{m_j=0}^J (2 - \delta_{m_j,0}) P_{\text{R}}(E_i, \nu, J, m_j)}{(2J + 1)} \quad (10)$$

The initial sticking probability  $S_0(\langle E_i \rangle)$  is then calculated as a function of average incidence energy  $\langle E_i \rangle$  by averaging over the rovibrational  $(\nu, J)$  states populated in the beam (see eq 8) and the flux-weighted distribution of the incidence translational energies of the beam according to

$$S_0(\langle E_i \rangle) = \sum_J \sum_{\nu} \frac{\int_0^{\infty} P'(E_i, \nu, J, T_n) R_{\text{mono}}(E_i, \nu, J) dE_i}{\int_0^{\infty} P'(E_i, \nu, J, T_n) dE_i} \quad (11)$$

We note that, although  $S_0(\langle E_i \rangle)$  is written and plotted in studies as a function of average incidence only, it also implicitly depends on  $T_n$  through the distribution  $P'(E_i, \nu, J, T_n)$  of incidence energies and the rovibrational state populations

$$P'(E_i, \nu, J, T_n) dE_i = P'_{\text{flux}}(E_i; T_n) dE_i \times P_{\text{int}}(\nu, J, T_n) \quad (12)$$

$P'(E_i, \nu, J, T_n)$  makes the initial sticking also depend implicitly on incident beam conditions other than just  $T_n$  due to the occurrence of the flux-weighted distribution of incidence

**Table 2. Molecular Beam Parameters Taken from Experiments Performed on the  $\text{H}_2(\text{D}_2) + \text{Cu}(111)$  System<sup>a</sup>**

| $T_n$ (K)  | $\langle E_i \rangle$ (kJ/mol) | $\nu_0$ (m/s) | $E_0$ (eV) | $\alpha$ (m/s) |
|--|--------------------------------|---------------|------------|----------------|
| Seeded molecular $\text{H}_2$ beams ( $T_s = 120$ K) |                                |               |            |                |
| 1740   | 19.9                           | 3923          | 0.160      | 1105           |
| 1740   | 28.1                           | 4892          | 0.250      | 1105           |
| 1740   | 38.0                           | 5906          | 0.364      | 945            |
| 2000   | 18.2                           | 3857          | 0.155      | 995            |
| 2000   | 25.1                           | 4625          | 0.223      | 1032           |
| 2000   | 44.1                           | 6431          | 0.432      | 886            |
| Seeded molecular $\text{D}_2$ beams ( $T_s = 120$ K) |                                |               |            |                |
| 2100   | 62.6                           | 5377          | 0.829      | 649            |
| 2100   | 69.2                           | 5658          | 0.860      | 717            |
| 2100   | 80.1                           | 6132          | 0.849      | 830            |
| Pure molecular $\text{H}_2$ beam ( $T_s = 120$ K)    |                                |               |            |                |
| 1435   | 31.7                           | 5417          | 0.307      | 826            |
| 1465   | 32.0                           | 5446          | 0.310      | 830            |
| 1740   | 38.0                           | 5906          | 0.364      | 945            |
| 1855   | 40.5                           | 6139          | 0.394      | 899            |
| 2000   | 44.1                           | 6431          | 0.432      | 886            |
| 2100   | 47.4                           | 6674          | 0.465      | 913            |
| 2300   | 49.7                           | 6590          | 0.454      | 1351           |
| Pure molecular $\text{H}_2$ beam (Rendulic et al.)   |                                |               |            |                |
| 1118.07  | 25.1                           | 3500          | 0.12794    | 1996           |
| 1331.89  | 29.9                           | 3555          | 0.13200    | 2342           |
| 1438.82  | 32.3                           | 3380          | 0.11932    | 2611           |
| 1501.19  | 35.7                           | 3151          | 0.10371    | 2819           |
| 1581.35  | 35.5                           | 3219          | 0.10816    | 2903           |

<sup>a</sup>The parameters are used in this work to simulate the reaction of molecular hydrogen on  $\text{Cu}(211)$  as it would occur in experiments analogous to those performed on  $\text{Cu}(111)$ . The parameters  $\nu_0$ ,  $\alpha$ ,  $T_n$  represent the stream velocity of the beam, the width of the beam, and the nozzle temperature at an average translational incidence energy  $\langle E_i \rangle$ , respectively. Parameters were taken from refs 15 and 34.

energies  $P'_{\text{flux}}(E_i; T_n)$ , which depends on a number of factors including the molecular beam geometry, backing pressure, and whether or not a seeding gas is used and can be described by the parameters  $E_0$  and  $\Delta E_0$  according to

$$P'_{\text{flux}}(E_i; T_n) dE_i = C' E_i e^{-4E_0(\sqrt{E_i} - \sqrt{E_0})^2 / \Delta E_0^2} dE_i \quad (13)$$

Instead of averaging over incidence energies using  $P'_{\text{flux}}(E_i; T_n)$  as done in eq 12, it is also possible to average over the flux-weighted velocity distribution of the molecules in the beam,  $P_{\text{flux}}(\nu; T_n)$ , and the derivation  $P'_{\text{flux}}(E_i; T_n)$  from  $P_{\text{flux}}(\nu; T_n)$  is discussed in ref 77. For a particle of mass  $m$ , the parameters are defined as  $E_0 = m\nu_0^2/2$  and  $\Delta E_0 = 2E_0\alpha/\nu_0$ .

To obtain sticking coefficients  $S_0$ , we perform 114 state-resolved calculations (corresponding to 342 wave packet calculations) for an energy range of  $E_i \in [0.05, 1.4]$  eV. The initial states of incident  $\text{H}_2$  considered here to evaluate eq 11 are characterized by the quantum numbers  $J \in [0, 11]$  for  $\nu = 0$  and  $J \in [0, 7]$  for  $\nu = 1$  and  $m_j \in [0, J]$ .

The rotational quadrupole alignment parameter as a function of  $\nu$  and  $j$  is a measure of the extent to which the reaction depends on the orientation of the molecule. The rotational quadrupole alignment parameter is calculated from the fully state-resolved reaction probability as follows<sup>78</sup>

$$A_0^{(2)}(\nu, J) = \frac{\sum_{m_j=0}^J (2 - \delta_{m_j,0}) P_r(\nu, J, m_j) \left( \frac{3m_j^2}{J(J+1)} - 1 \right)}{\sum_{m_j=0}^J (2 - \delta_{m_j,0}) P_r(\nu, J, m_j)} \quad (14)$$

### 3. RESULTS AND DISCUSSION

**3.A. Fully State-Resolved Reaction Probabilities.** In order to highlight the difference between a QD and QCT treatment of the  $\text{H}_2 + \text{Cu}(211)$  system, we first present initial state-resolved reaction probabilities in Figure 2a–c. QD

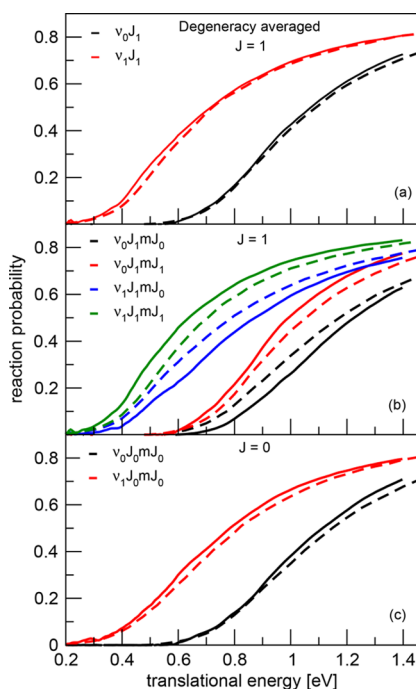


**Figure 2.** Reaction probability computed with QD calculations (solid lines) and QCT calculations (dashed lines) for normal incidence. Panel (a) shows degeneracy averaged reaction probabilities for  $J = 1$  for both the ground state and the first vibrationally excited state. Panel (b) shows the  $m_j = 0, 1$  states belonging to  $J = 1$  for both the ground state and the first vibrationally excited state. Panel (c) shows the  $J = 0$  state for both the ground state and the first vibrationally excited state as well.

calculations have been performed for a large number of rovibrational states. All input parameters can be found in Table 1. The biggest differences between QD and QCT calculations at the fully state-resolved level are observed for the lowest rovibrational states, as shown in Figure 2b,c. The differences get increasingly smaller with increasing  $J$  for  $J > 1$ . From QCT data at higher translational energies that are not shown in this figure, it is clear that all states converge toward an asymptotic maximum reaction probability, which depends slightly on the rovibrational state with respect to the maximum reaction probability. We note that for a very high  $J$ ,  $J > 10$  (not shown here), QD predicts a marginally smaller (less than 2%) asymptotic maximum reaction probability, while Figure 2c suggests that the opposite is true for the vibrational ground state and the first vibrationally excited state.

Figure 2b shows the largest discrepancy between the QCT and QD calculations observed. Here,  $|m_j| = J$  pertains to a “helicoptering”  $\text{H}_2$  molecule, and  $m_j = 0$  pertains to a

“cartwheeling”  $\text{H}_2$  molecule rotating in a plane perpendicular to the surface normal. The preference for reacting parallel to the surface (i.e.,  $m_j = J$  having a higher reaction probability than  $m_j = 0$ ) is bigger for QD calculations than QCT calculations. This difference is negligible, however, when looking at degeneracy averaged reaction probabilities, which are shown in Figure 2a. This also holds for the states not shown here. When looking at degeneracy averaged reaction probabilities, the agreement between the QCT and QD method is excellent.

In our calculations, we see no evidence of the “slow channel” reactivity reported by Kaufmann et al.<sup>45</sup> in their very recent paper, that is, reaction at low translational energies. We can now rule out quantum effects during the dynamics as the source of this slow channel reactivity, in which the reaction supposedly is inhibited by translational and promoted by vibrational energy.<sup>45</sup> When looking at the individual rovibrational states that exhibit the biggest difference in reactivity between QD and QCT calculations, no evidence of the slow reaction channel is present in our results. The translational energy range sampled in our calculations should overlap with the translational energy range where the slow channel is reported to be active by Kaufmann et al.<sup>45</sup> We therefore propose that the observed slow reaction channel must originate from surface motion at a very high surface temperature (923 K), which has not been incorporated into our QD calculations and is challenging to incorporate in QCT calculations.<sup>79</sup>

### 3.B. Rotational Quadrupole Alignment Parameters.

As might be suspected from Figure 2b from the larger preference for a parallel reaction orientation for  $J = 1$ , calculated rotational quadrupole alignment parameters show a large difference between QCT and QD calculations for the  $J = 1$  states shown there. However, here, we will now focus on rotational quadrupole alignment parameters for two particular rovibrational states of  $\text{H}_2$ , ( $\nu = 0, J = 7$ ) and ( $\nu = 1, J = 4$ ) (Figure 3a), and those of  $\text{D}_2$ , ( $\nu = 0, J = 11$ ) and ( $\nu = 1, J = 4$ ) (Figure 3b). These two sets of states were selected because they are very similar in rotational energy to the two rovibrational states for which rotational quadrupole alignment parameters for  $\text{D}_2$  desorbing from  $\text{Cu}(111)$  have been measured experimentally<sup>16</sup> and studied theoretically using the BOMD method.<sup>32</sup> Results for both states of  $\text{D}_2$  reacting on  $\text{Cu}(111)$  have been included in Figure 3b. Note that a positive  $A_0^{(2)}(\nu, J)$  indicates a preference for a parallel reaction orientation, a negative value indicates a preference for a perpendicular orientation, and zero means the reaction proceeds independent of the orientation.

We observe that the predicted rotational quadrupole alignment parameters eventually tend to zero with increasing translational energy, as all molecules irrespective of the orientation will have enough energy to traverse the barrier. It is also clear that for  $\text{H}_2$  ( $\nu = 0, J = 7$ ), the agreement between QCT and QD calculations is excellent. The slight deviations at the lowest translational energies can be attributed to noise in the very low reaction probabilities of the underlying individual states.

The increase in the rotational quadrupole alignment parameter with decreasing translational energy, for the  $\text{H}_2$  ( $\nu = 0, J = 7$ ) and  $\text{D}_2$  ( $\nu = 0, J = 11$ ) states, is comparable to what is reported in the literature for  $\text{H}_2$  and  $\text{D}_2$  associatively desorbing from  $\text{Cu}(111)$  and  $\text{Cu}(100)$ .<sup>16,30–32</sup> This monotonic increase in the rotational quadrupole alignment parameter with decreasing translational energy can be

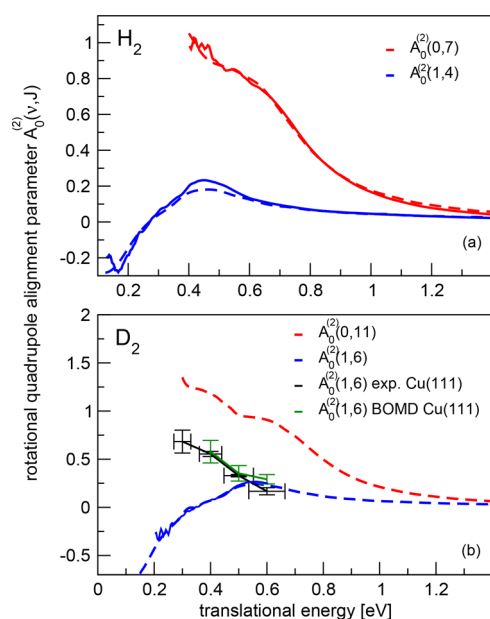


**Figure 3.** Panel (a) shows rotational quadrupole alignment parameters,  $A_0^{(2)}(\nu, J)$ , for two rovibrational states of  $H_2$ : ( $\nu = 0, J = 7$ ) and ( $\nu = 1, J = 4$ ). Panel (b) shows rotational quadrupole alignment parameters for two rovibrational states of  $D_2$ : ( $\nu = 0, J = 11$ ) and ( $\nu = 1, J = 6$ ). Solid lines correspond to QD calculations, and dashed lines correspond to QCT calculations. Panel (b) also shows experimental results for  $D_2$  on Cu(111) (black line)<sup>16</sup> and BOMD results for  $D_2$  ( $\nu = 1, J = 6$ ) on Cu(111) (green line).<sup>32</sup>

explained by a static effect of orientational hindering, in which slow- or nonrotating molecules will scatter when their initial orientation does not conform to the lowest barrier geometry.<sup>31</sup> Specifically, the molecule must be in favorable orientation to begin with in order to react, especially with the energy available to reaction being close to the threshold energy.

The blue lines in Figure 3a correspond to the ( $\nu = 1, J = 4$ ) rovibrational state of  $H_2$  and those in Figure 3b to the ( $\nu = 1, J = 6$ ) rovibrational state of  $D_2$ . In contrast to the previously described states ( $\nu = 0$ , high  $J$ ), the rotational quadrupole alignment parameter now first increases with increasing translational energy until reaching a maximum around 0.43 eV for  $H_2$  and 0.52 eV for  $D_2$  before decreasing toward zero with increasing translational energy. From Figure 3, it is clear that, around the maximum, the agreement between the QD and QCT calculations is not as excellent for  $H_2$  than  $D_2$ , although the agreement is still good.

The downturn of the rotational quadrupole alignment parameter with decreasing translational energy seen here for  $D_2$  and  $H_2$  in their ( $\nu = 1$ ) states colliding with Cu(211) was not observed for  $D_2$  desorbing from Cu(111) for which, as can be seen in Figure 3b, only a monotonous increase with decreasing translational energy has been reported.<sup>16,32</sup> A slight downturn of the rotational quadrupole alignment parameters has been predicted for vibrationally excited  $H_2$  reacting on Cu(100),<sup>30,31</sup> although the downturn was too small to lead to a negative rotational quadrupole alignment parameter. Because the behavior predicted for ( $\nu = 1$ ) hydrogen colliding with Cu(211) qualitatively differs from that observed previously for Cu(111) and Cu(100), we will now first attempt to explain the dependence of the rotational quadrupole alignment parameter on incidence energy that we predict for  $D_2$  ( $\nu = 1, J = 6$ ) and then discuss the case of  $D_2$  ( $\nu = 0, J = 11$ ).

From the literature, it is known that the behavior of the rotational quadrupole alignment parameter as a function of incidence energy can be related to features of the molecule–surface interaction at the preferred reaction site of the molecule for the initial rovibrational state considered.<sup>31</sup> For example, vibrationally excited  $H_2$  with a translational energy close to the threshold to reaction was found to prefer to react on a top site of Cu(100) due to features in the PES being more favorable; for instance, the increased lateness of the barrier at this site allowed more efficient conversion of energy from vibration to motion along the reaction path.<sup>31,37,38</sup> Next, the dependence of the rotational quadrupole alignment parameter on incidence energy of vibrationally excited  $H_2$  on Cu(100) could be explained on the basis of the anisotropy of the molecule–surface interaction energy at the top site. In our explanation of the behavior seen for  $H_2$  and  $D_2$  on Cu(211), we will therefore proceed in a similar manner.

Figure 4a shows the reaction density of  $D_2$  ( $\nu = 1, J = 6$ ) extracted from QCT calculations projected onto the Cu(211)

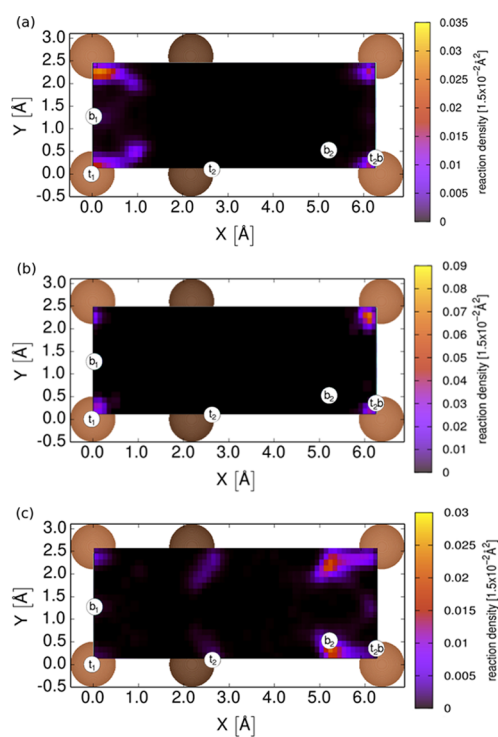


**Figure 4.** Three plots of the reaction density of  $D_2$  projected onto the Cu(211) unit cell. Panel (a) shows the reaction density of  $D_2$  ( $\nu = 1, J = 6$ ); all reacted trajectories up to a translational energy of 0.35 eV are included. Panel (b) shows the reaction density of  $D_2$  ( $\nu = 0, J = 11$ ); all reacted trajectories up to a translational energy of 0.35 eV are included. Panel (c) shows the reaction density of  $D_2$  ( $\nu = 0, J = 2$ ); all reacted trajectories up to a translational energy of 0.65 eV are included.

unit cell. Here, we focus specifically on the  $D_2$  ( $\nu = 1, J = 6$ ) rovibrational state because it has been experimentally measured on Cu(111),<sup>16</sup> but the same mechanism appears to be present in our data for  $H_2$  ( $\nu = 1, J > 2$ ). All reacted trajectories up to a translational energy of 0.35 eV have been included. It is immediately clear that molecules in this particular state prefer to react on the  $t_1$  top site,<sup>46</sup> which, in the case of Cu(211), is at the step, with small outliers in reactivity pointing toward the bottom of the step. The  $t_1$

barrier is an extremely late barrier ( $r_{t_1} = 1.44 \text{ \AA}$ ), as can be seen in Table 3 of ref 46. The very late barrier allows for efficient conversion of vibrational energy to motion along the reaction coordinate.<sup>10,11,40</sup>

Figure 5 shows a representative reactive trajectory of  $D_2$  ( $\nu = 1, J = 6, m_j = 0$ ) with a translational energy of 0.3 eV and plots

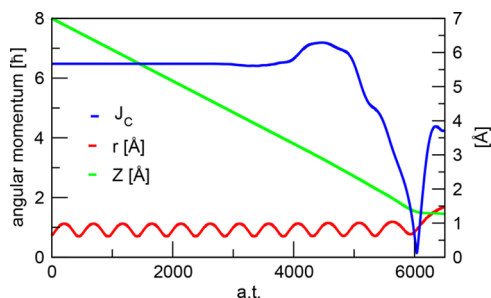


**Figure 5.** Single representative reactive trajectory of  $D_2$  ( $\nu = 1, J = 6, m_j = 0$ ) with a translational energy of 0.3 eV. Blue shows the angular momentum ( $J_C$ ), red shows the bond length ( $r$ ), and green shows the center of mass distance to the surface ( $Z$ ).

the classical angular momentum,  $J_C$ , as a function of the propagation time.  $J_C$  is decreased before reaching the barrier, and a minimum in  $J_C$  is reached at the transition state, where  $r$  becomes equal to  $1.44 \text{ \AA}$  corresponding to the  $t_1$  barrier.<sup>46</sup> In the majority of the reacted trajectories, the minimum of  $J_C$  is reached when  $r$  reaches the value of the  $t_1$  transition state, even when the molecule would make one or more bounces on the surface. This is a clear indication that rotational de-excitation takes place before the molecule reaches the transition state. This suggests that the reaction proceeds through rotational inelastic enhancement,<sup>31</sup> that is, the reaction is promoted by rotational energy flowing to the reaction coordinate. The bump in  $J_C$  (i.e., its increase) still relatively far away from the surface is a feature that is also present in the majority of reactive trajectories. It is not completely clear to us what the cause is of this increase in  $J_C$  still relatively far away from the surface before proceeding toward the transition state. We speculate that the increasing vicinity to the surface turns on the anisotropy of the molecule–surface interaction, thereby coupling rotational motion and stretching motion and providing a mechanism for the rotational energy to remain more constant while the bond extends and compresses due to the molecular vibration. This mechanism could consist in the classical angular momentum increasing when the bond extends to offset the effect of the bond extension on the rotational constant (upon bond extension the rotational constant decreases and, if not compensated, this would decrease the rotational energy). This could possibly explain the hump observed in  $J_C$  at  $t \approx 4500$  atomic units of time in Figure 5.

There is also indirect evidence for rotationally enhanced reaction of  $D_2$  ( $\nu = 1, J = 6, m_j = 0$ ) in our QD calculations. Figure 6a shows inelastic scattering probabilities for  $D_2$  ( $\nu = 1, J = 6, m_j = 0$ ), and Figure 6b shows inelastic scattering probabilities for  $D_2$  ( $\nu = 1, J = 6, m_j = 6$ ). From a pairwise comparison of data with the same color between Figure 6a and Figure 6b, it is clear that  $D_2$  ( $\nu = 1, J = 6, m_j = 0$ ) has a considerably higher probability to rotationally de-excite in the scattering process compared to  $D_2$  ( $\nu = 1, J = 6, m_j = 6$ ). This suggests that the reaction of ( $\nu = 1, J = 6, m_j = 0$ ) is also rotationally enhanced in the quantum dynamics if the de-

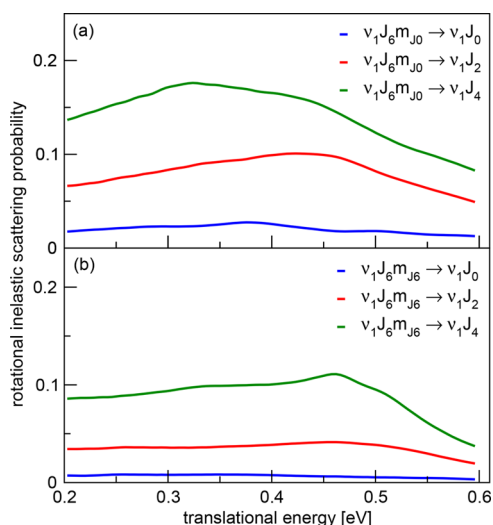


**Figure 6.** Rotational inelastic scattering probabilities for  $D_2$  for two different initial rovibrational states as a function of translational energy. Panel (a) shows rotational inelastic scattering probabilities for  $D_2$  ( $\nu = 1, J = 6, m_j = 0$ ). Panel (b) shows rotational inelastic scattering probabilities for  $D_2$  ( $\nu = 1, J = 6, m_j = 6$ ). Colors correspond to the final rovibrational state of the molecule, with blue being ( $\nu = 1, J = 0$ ), red being ( $\nu = 1, J = 2$ ), and green being ( $\nu = 1, J = 4$ ).

excitation occurs before the barrier is reached and the released rotational energy is transferred to motion along the reaction coordinate.

There are four possible mechanisms that affect the reaction probability and may affect the rotational quadrupole alignment parameters: two enhancing mechanisms and two steric hindering mechanisms.<sup>31</sup> Here, we have focused on one enhancement mechanism, inelastic rotational enhancement, since the evidence presented in Figures 5 and 6a,b is consistent with this mechanism. Inelastic rotational enhancement requires the reaction to take place on a site with a low anisotropy in  $\phi$  and a large anisotropy in  $\theta$  at the barrier.<sup>31</sup> The main reasons for proposing the presence of this mechanism are the sharp downturn of the quadrupole alignment parameters for ( $\nu = 1, J > 2$ ) rovibrational states in Figure 3a,b and the rotational de-excitation seen in Figures 5 and 6a,b. We note that inelastic rotational enhancement is the only mechanism that predicts a lowering of the rotational quadrupole alignment parameters.<sup>31</sup> A complete overview of the four mechanisms and what features of the PES they depend on can be found in Table III of ref 31.

A feature of the  $t_1$  site that facilitates the conversion of rotational energy to motion along the reaction coordinate is a low anisotropy of the potential in  $\phi$  combined with a large anisotropy in  $\theta$ . Figure 7 shows the anisotropy at the  $t_1$  barrier<sup>46</sup> ( $r$  and  $Z$  are kept constant here), the top panel shows the anisotropy in  $\phi$ , and the bottom panel shows the anisotropy in  $\theta$ . It is clear that the anisotropy in  $\theta$  is substantial, while the anisotropy in  $\phi$  is very small compared to the anisotropy in  $\theta$ . Somers et al.<sup>31</sup> have shown that the high anisotropy in  $\theta$  may facilitate inelastic rotational enhancement. Inelastic rotational enhancement is expected to be most effective for low  $|m_j|$  states with  $J > 2$ , and the mechanism would lead to decreased rotational quadrupole alignment parameters.<sup>31</sup> The reason for the decrease in the rotational quadrupole alignment parameters is that  $m_j$  is approximately conserved, so that a decrease in  $J$  is possible only for a low  $|m_j|$ .



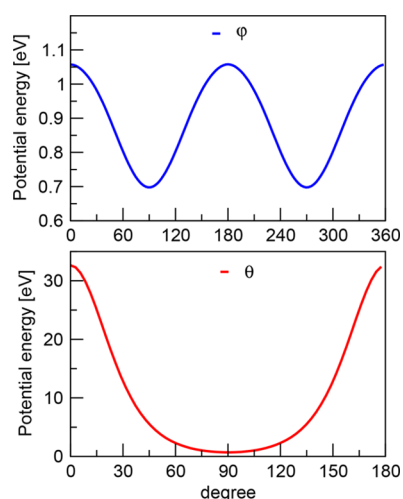


**Figure 7.** Anisotropy of the interaction potential at the  $t_1$  top site barrier<sup>46</sup> for  $\theta$  (top panel) and  $\phi$  (bottom panel).

It is also clear from Figure 3b that from the point of view of the orientational dependence of reaction, Cu(211) cannot be described as a combination of (100) steps and (111) terraces. The monotonic increase in the rotational quadrupole alignment parameter for  $D_2$  reacting on Cu(111)<sup>16,32</sup> is very similar to the behavior reported for Cu(100).<sup>30,31</sup> A slight downturn at translational energies close to the threshold to reaction has been reported in the case of Cu(100), indicating that the inelastic rotational enhancement mechanism is taking place. The downturn is however small and does not lead to negative quadrupole alignment parameters as we show here for  $H_2$  and  $D_2$  reacting on Cu(211). This is a clear indication that the reaction dynamics of the Cu(211) surface are distinct from the reaction dynamics of its component Cu(111) terraces and Cu(100) steps when looked at individually. This is most likely because the energetic corrugation of the Cu(211) surface is much lower compared to Cu(111) and Cu(100), a feature that favors the reaction of vibrationally excited molecules if sites with late barriers are present.

We now turn to an explanation for the monotonic decrease in the rotational quadrupole alignment parameter predicted for the ( $\nu = 0$ , high  $J$ ) states of  $H_2$  and  $D_2$  colliding with Cu(211) in Figure 3a,b. No downturn of the rotational quadrupole alignment parameter is observed for the ( $\nu = 0$ ) states even though  $D_2$  ( $\nu = 0$ ,  $J = 11$ ,  $m_j = 11$ ) reacts at the step as well as  $D_2$  ( $\nu = 1$ ,  $J = 6$ ), as can be seen in Figure 4b. The lack of a downturn in the rotational quadrupole alignment parameter arises because the  $D_2$  ( $\nu = 0$ ) states react using a different mechanism. Figure 8 shows a representative reactive trajectory of  $D_2$  ( $\nu = 0$ ,  $J = 11$ ,  $m_j = 11$ ), and it is clear that the angular momentum only drops after the transition state has been reached. This is a clear combination of elastic rotational enhancement for the helicopter molecules together with orientational hindering for the cartwheeling molecules, which causes the increase in the rotational quadrupole alignment parameters of the ( $\nu = 0$ ) molecules.<sup>31</sup> We note that  $D_2$  ( $\nu = 0$ ,  $J = 11$ ) reacting on the step at the  $t_1$  site is due to the high initial rotational quantum number. The  $t_1$  barrier is slightly higher in energy than the lowest barrier to the reaction, but at this site, the reaction is less rotationally hindered if the molecule rotates in a plane parallel to the surface, and the barrier is much later than at the lowest  $b_2$  barrier on the

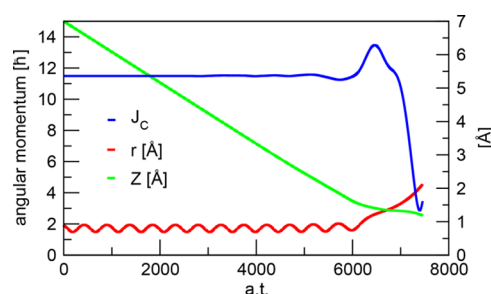


**Figure 8.** Single representative reactive trajectory of  $D_2$  ( $\nu = 0$ ,  $J = 11$ ,  $m_j = 11$ ) with a translational energy of 0.3 eV. Blue shows the angular momentum ( $J_c$ ), red shows the bond length ( $r$ ), and green shows the center of mass distance to the surface ( $Z$ ).

terrace. This allows molecules in the vibrational ground state that are rotating fast in helicopter fashion and have incidence energies close to the threshold to reaction to react there by converting rotational energy to motion along the reaction path as the bond extends and the rotational constant of the molecule drops, while  $j$  remains roughly the same.

Above, we have shown that  $D_2$  in its ( $\nu = 0$ ,  $J = 11$ ) and ( $\nu = 1$ ,  $J = 6$ ) states prefers to react near the  $t_1$  site, that is, on or near the steps (see Figure 4a,b). This might seem to contradict an earlier conclusion that, at low incidence energies,  $D_2$  prefers to react on the terrace.<sup>46</sup> However, this conclusion was based on molecular beam experiments and simulations of those experiments, and under the conditions addressed,<sup>46</sup> the ( $\nu = 0$ ,  $J = 11$ ) and ( $\nu = 1$ ,  $J = 6$ ) states would hardly have population in them. A more appropriate picture of the reaction density for molecules under the conditions of ref 46 is shown in Figure 4c. There, it can be seen that  $D_2$  ( $\nu = 0$ ,  $J = 2$ ) (this state would be highly populated in the beams used and simulated in ref 46) prefers to react at the terrace  $b_2$  site, which has the lowest barrier to the reaction. The reaction density for  $D_2$  ( $\nu = 0$ ,  $J = 2$ ) is in line with earlier findings that molecules in the vibrational ground state with low  $j$  react at the lowest barrier to the reaction<sup>31,37,38</sup> as well as with the findings for  $D_2 + Cu(211)$  of ref 46.

Kaufmann et al.<sup>45</sup> did not measure rotational quadrupole alignment parameters in their recent study. We believe that the downturn of the rotational quadrupole alignment parameter at low incidence energies, which has not been observed before with this large downward shift for both  $H_2$  and  $D_2$  reacting on copper, may well be experimentally verified for both isotopes on Cu(211). Specifically, the reaction probability of  $H_2$  and  $D_2$  is large enough, and the ( $\nu = 1$ ,  $J = 4$ ) rovibrational state of  $H_2$  and the ( $\nu = 1$ ,  $J = 6$ ) state of  $D_2$  have large enough Boltzmann weights at reasonable surface temperatures (923 K) to make the downturn measurable. Comparing experimental rotational quadrupole alignment parameters to theoretical ones will provide a very stringent and detailed way of testing the accuracy of the electronic structure calculations used in the construction of the PES.

### 3.C. Comparing to Experimental $E_0(\nu, J)$ Parameters.

Next, we will make a direct comparison with the state-specific, or degeneracy averaged, reaction probabilities reported by Kaufmann et al.<sup>45</sup> From their experiments, they could derive dissociative adsorption probabilities by applying the principle of detailed balance to the measured time-of-flight distributions. However, comparing the relative saturation value of the reaction probability obtained from associative desorption experiments to the zero coverage absolute saturation values

predicted by theory is not straightforward. The authors of the experimental paper pose several ways of scaling the experimental data in order to make a comparison to theoretical work possible. Scaling the experimental data to experimental molecular adsorption results introduces the uncertainties related to the direct molecular adsorption experiment used as a reference in this process. Theory calculates sticking probabilities in the zero coverage limit. When scaling the experimental desorption data to the experimental adsorption data, the zero coverage limit will only be a lower bound, especially when a molecular beam experiment with a very broad translational energy distribution is chosen as a reference.

We opt for the simplest and most direct method to scale to the relative experimental associative desorption data. In order to compare to the experimental  $E_0(\nu, J)$  parameters, where  $E_0(\nu, J)$  is the translational energy for which the reaction probability of the  $(\nu, J)$  state is half of the maximum reaction probability measured for the  $(\nu, J)$  state, we use the maximum translational energy sensitivity reported in Tables S7 and S9 of ref 45. Theoretical  $E_0(\nu, J)$  are taken to be the translational energy to which the reaction probability is half that of the reaction probability at the maximum translational energy for which the experiment is sensitive. This method also corresponds to what is showcased in Figure 13a of ref 45.

Figure 9 shows  $E_0(\nu, J)$  parameters for  $H_2$  and  $D_2$  reacting on Cu(211). The agreement between the theory and

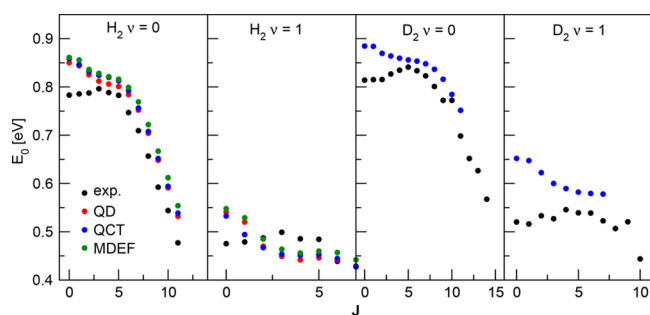


**Figure 9.**  $E_0(\nu, J)$  parameters as a function of  $J$  for  $H_2$  and  $D_2$  reacting on Cu(211). Blue dots represent QCT results, red dots represent QD results, green dots represent MDEF results, and black dots represent experimental results.<sup>45</sup>

experiment is excellent for  $H_2$ . We calculated mean absolute and mean signed deviations between the experimental and theoretical  $E(\nu, J)$  parameters (see Table 3). It is clear from Figure 9 and Table 3 that the agreement between the theory and experiment is excellent in the case of  $H_2$ , for which the total mean absolute deviation (MAD) ( $n^{-1} \sum_n |E_{0, \text{exp}, n} - E_{0, n}|$ )

) and mean signed deviation (MSD) ( $n^{-1} \sum_n E_{0, \text{exp}, n} - E_{0, n}$ ) values for QD and QCT calculations fall within chemical accuracy. We note that, for  $H_2$ , the agreement is best for vibrationally excited molecules, while the reverse is true with respect to  $D_2$ . For  $D_2$ , the agreement is not yet within the chemical accuracy, mainly due to the slightly bigger discrepancies between the theory and experiment for the first vibrationally excited state. The theory, however, does not reproduce the rotational hindering that can be seen in the experimental data, that is,  $E_0(\nu, J)$  does not first increase with  $J$  until a maximum before falling off with increasing  $J$ . The theory shows no such behavior; here, the  $E_0(\nu, J)$  parameter falls off with increasing  $J$  for all methods investigated here.

Experiments on associative desorption of  $H_2$  from Cu(111)<sup>18,45</sup> and that of  $D_2$  from Cu(111)<sup>15,32,45</sup> likewise found the rotational hindering effect on reaction for low  $j$ . As for  $H_2$  and  $D_2$  interacting with Cu(211), we have not been able to reproduce this subtle effect in calculations on  $H_2 + \text{Cu}(111)$ <sup>34,35</sup> and  $D_2 + \text{Cu}(111)$ <sup>32,34</sup> in electronically adiabatic dynamics calculations. Here, we find that MDEF calculations on  $H_2$  and  $D_2 + \text{Cu}(211)$  do not reproduce the trend either, suggesting that, in the previous calculations, neglecting electron–hole pair excitation was not the cause of the discrepancy between the theory and experiment. However, it is possible that calculations modeling electron–hole pair excitation with orbital-dependent friction (ODF) will succeed in recovering the subtle trend observed in experiments. For this, it may well be necessary that the ODF coefficients explicitly model the dependence of the tensor friction coefficients on the molecule’s orientation angles; earlier MDEF calculations on  $H_2 + \text{Cu}(111)$  using ODF coefficients have not yet done this.<sup>25</sup>

According to Figure 9, the reactivity measured experimentally in the associative desorption experiments is, for most  $(\nu, J)$  states, larger than that predicted theoretically, with the experimental  $E_0(\nu, J)$  being lower. With the use of the same scaling method to relate theory to experiment, Kaufmann et al.<sup>45</sup> obtained the same result for  $H_2$  and  $D_2$  reacting on Cu(111), and also in their case, they compared theory on the SRP48 functional.<sup>32</sup> To some extent, these results are odd, as calculations for  $H_2$  and  $D_2 + \text{Cu}(111)$  using the original SRP functional showed that the theory overestimated the experimentally measured sticking coefficients.<sup>35</sup> However, also in this work, the theory generally underestimated the reactivity measured in associative desorption experiments.<sup>35</sup>

The paradox noted above may be explained on the basis of the BOSS model used in the calculations. This model neglects the effect of ehp excitation. Modeling this effect on sticking experiments should lower the theoretical reactivity, with

**Table 3.** Mean Absolute and Mean Signed Deviations for the Theoretical  $E_0(\nu, J)$  Parameters Compared to Experimental Values Shown in Figure 9

| parameters     | MAD (eV) $H_2$ |           |           | MSD (eV) $H_2$ |           |           |
|----------------|----------------|-----------|-----------|----------------|-----------|-----------|
|                | total          | $\nu = 0$ | $\nu = 1$ | total          | $\nu = 0$ | $\nu = 1$ |
| QCT            | 0.0362         | 0.0384    | 0.0289    | 0.0209         | 0.0384    | −0.0044   |
| QD             | 0.0362         | 0.0449    | 0.0235    | 0.0241         | 0.0449    | −0.006    |
| MDEF           | 0.0509         | 0.0531    | 0.0272    | 0.0342         | 0.0532    | 0.0069    |
| MDEF*          | 0.0239         | 0.0237    | 0.0306    | 0.0076         | 0.0236    | −0.0157   |
| MAD (eV) $D_2$ |                |           |           |                |           |           |
| parameters     | MAD (eV) $D_2$ |           |           | MSD (eV) $D_2$ |           |           |
|                | total          | $\nu = 0$ | $\nu = 1$ | total          | $\nu = 0$ | $\nu = 1$ |
| QCT            | 0.0485         | 0.0354    | 0.0675    | 0.0485         | 0.0354    | 0.0675    |

computed sticking curves shifting to higher energies. Modeling the effect on associative desorption experiments should show the opposite effect if the modeling is done correctly, that is, starting with molecules being formed at the transition state and then desorbing.<sup>35,80</sup> The effect of ehp excitation in such calculations should lead to translational energy distributions of desorbed molecules being shifted to lower translational energies. The reaction probability curves obtainable from these distributions by assuming detailed balance (which, strictly speaking, is not applicable if ehp excitation is active) should then lead to computed reaction probability curves ( $E_0(\nu, J)$  values) shifted toward lower energies, in better agreement with the experiment (see Figure 9).

The above also explains why our present MDEF calculations led to decreased agreement with the experiment: In these calculations, we modeled the associative desorption experiment as an initial-state selected dissociative chemisorption experiment, in which ehp excitation should have the opposite effect. If we assume the ehp excitation to have an effect that is similar in magnitude but opposite in sign with respect to the QCT calculations, then the net effect of modeling ehp excitation is to increase the agreement with the experiment to the extent that chemical accuracy is obtained for both ( $\nu = 0$ ) and ( $\nu = 1$ )  $H_2$  on Cu(211). This is illustrated by the MDEF\* mean absolute and mean signed deviations in Table 3. The MDEF\* values have been calculated by subtracting the difference between the MDEF and QCT values from the QCT values. We finally note that we have assumed that the surface temperature does not much affect the measured  $E_0(\nu, J)$  through surface atom vibrational motion, which is in line with experiments,<sup>23,24</sup> as discussed in the Supporting information of Diaz et al.<sup>35</sup>

**3.D. Classical Molecular Beam Simulations.** One of the goals of this project was to carry out a molecular beam simulation using the QD method. Since surface atom motion and ehp excitations cannot be incorporated in QD calculations, we have also performed molecular beam simulations using the BOMD, QCT, and MDEF methods for  $D_2$  impinging on Cu(211) in order to quantify their effects on the reactivity measured in a molecular beam experiment. As discussed together with the comparison between our state-resolved reaction probabilities and the associative desorption experiments of Kaufmann et al.,<sup>45</sup> there are some effects on the reactivity from surface atom motion and ehp excitations though the effect falls within chemical accuracy. The molecular beam experiments we treat here were carried for a surface temperature of 120 K.<sup>15,34</sup>

In Figure 10, we compare BOMD calculations performed for a surface temperature of 120 K (red) to QCT (black) and MDEF (green) calculations carried out on our six-dimensional PES. As an additional validation of the PES, we have also calculated one energy point using the BOMD method with a rigid surface (blue). Each BOMD point is based on 500 trajectories, each QCT and MDEF point on 100,000 trajectories. The molecular beam parameters were taken from refs 15 and 35 and can be found in Table 2. From the excellent agreement in Figure 10 between the black and blue data points at 80.1 kJ/mol, it is clear that our PES was accurately fitted, as was previously demonstrated in Figure S2 of ref 46. There we showed that for the dynamically relevant region of the PES ( $V_{MAX} < 2$  eV), the PES has an RMSE of  $< 0.035$  eV. Therefore, results obtained from QD calculations performed on our PES should not be influenced much by any (small) lingering inaccuracies still present in the PES related to the fitting

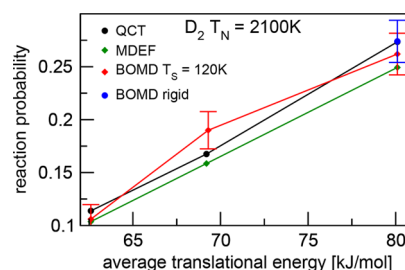


**Figure 10.** Reaction probability as function of the average translational energy for  $D_2$  on Cu(211), with molecular beam parameters taken from Table 2. BOMD results with a surface temperature of 120 K are shown in red, MDEF results are shown in green, and QCT results are shown in black. The blue point is a BOMD result for  $D_2$  on Cu(211) with a rigid surface.

procedure. It can also be observed from Figure 10 that the effect of surface motion is small and well within the limits of chemical accuracy with respect to incidence energy. Due to the fact that  $H_2$  has a lower mass, we expect that the effect of including surface motion during the dynamics will be even less pronounced for  $H_2$  than  $D_2$ . We should also note here that when low surface temperature experiments are considered, as with the 120 K surface temperature here, it is known from the literature that the BOSS model works well for activated  $H_2$  dissociation on metals.<sup>26,33,34,36,60</sup>

It can also be seen from Figure 10 that including the effect of ehp's as a classical friction force shifts the reaction probability curve slightly to higher energies and that the effect is rather small and linear with respect to the average translational energy. From the literature, it is also known that including ehp excitations in the dynamics of  $H_2$  reacting on Cu(111) has only a marginal effect on the reaction probability.<sup>25,32,36,81</sup>

Due to the very small contribution of surface atom motion and nonadiabatic effects incorporated in the MDEF calculations to the overall reaction probability, we pose that  $H_2$  impinging on Cu(211) is an excellent system to fully simulate a molecular beam experiment using quantum dynamics methods since large discrepancies between the theory and experiment can reasonably be attributed to quantum effects during the dynamics, as the BOSS model should be quite accurate.

**3.E. Quantum Molecular Beam Simulations.** Figure 11 shows results of simulations for four sets of molecular beam experiments, with varying molecular beam conditions. The experiment of Rendulic et al.<sup>14</sup> has the broadest translational energy distributions. The molecular beam parameters are taken from (the supporting information of) refs 15 34, and 35. Here, theoretical results obtained for the  $H_2 + Cu(211)$  system are compared to theoretical results for the  $H_2 + Cu(111)$  system, where, for all theoretical results, the SRP48 density functional was used. We only make a comparison to the theoretical work since, to the best of our knowledge, there exists no published experimental molecular beam dissociative adsorption data for  $H_2$  reacting on Cu(211).

In order to make the best possible comparison between the QCT and QD results, both results are calculated from initial state-resolved reaction probabilities for the same set of initial states. The molecular beam reaction probabilities predicted by QCT and QD calculations are in excellent agreement (Figure 11). The excellent agreement holds for the very broad molecular beams of Rendulic et al. in Figure 11a as well as for the translationally narrow molecular beams of Auerbach et al.<sup>15</sup> shown in Figure 11b–d. However, QCT predicts slightly

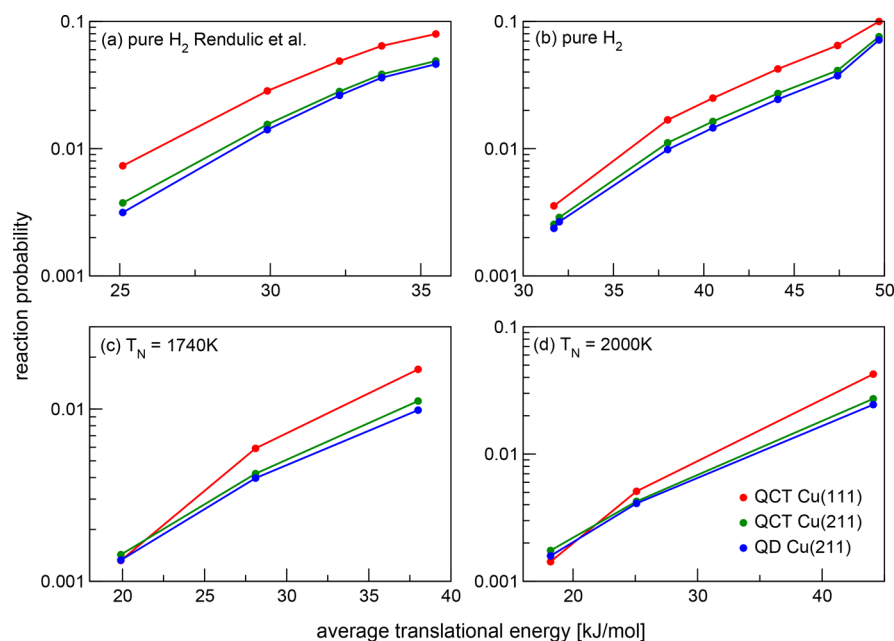


**Figure 11.** Comparison between four sets of molecular beam simulations for H<sub>2</sub> + Cu(111) and Cu(211), using the SRP48 functional, and for normal incidence. Reactivity is shown as a function of average translational energy. The red dots correspond to QCT calculations for H<sub>2</sub> + Cu(111). The green and blue dots correspond to the QCT and QD calculations for H<sub>2</sub> + Cu(211), respectively.

higher reaction probabilities, especially for the lowest translational energies. The consistently higher QCT reaction probability can be attributed to zero-point energy (ZPE) leakage, which is not possible by design in the QD calculations wherein the ZPE is preserved.

The excellent agreement between the QCT and QD calculations implies that, on the scale of a molecular beam experiment, in which a large number of rovibrational states are populated, quantum effects during the dynamics affect the reaction probability only in a very limited manner for reaction probabilities (>0.1%). The similarity between the QCT and QD calculations also holds over a wide range of molecular beam conditions, ranging from high to low incidence energies and from high to low nozzle temperatures.

From Figure 11, it is also clear that for most incidence energies (>22 kJ/mol), Cu(211) is predicted to be less reactive than Cu(111), as was reported previously for D<sub>2</sub> + Cu(211).<sup>46</sup> The lower reactivity of Cu(211) compared to Cu(111) cannot be explained by the d-band model.<sup>54,55</sup> In our previous paper, we and others showed that the d-band model does make accurate predictions of the reactivity of different facets when similar reaction geometries are considered but the breakdown of the predictive prowess of the d-band model is caused by the geometric effect of the lowest barrier to the reaction of H<sub>2</sub> dissociation on the low index Cu(111) surface not being on a top site.

Based on the results in Figure 11, we can now say definitively that, on the scale of a molecular beam experiment, neglecting quantum effects during the dynamics cannot be invoked to explain the lower reactivity of Cu(211) than Cu(111). This corroborates the theoretical results obtained in previous works,<sup>44,46</sup> where QCT calculations were performed for D<sub>2</sub> and H<sub>2</sub>, and S<sub>0</sub> values were measured for D<sub>2</sub> + Cu(111) for E<sub>i</sub> > 27 kJ/mol. More generally, we can state that molecular beam sticking of H<sub>2</sub> on cold Cu(211) is well described with quasi-classical dynamics, and this very probably also holds for H<sub>2</sub> reacting on Cu(111) and Cu(100).

#### 4. CONCLUSIONS

In this work, we have carried out a comprehensive study of the quantum reaction dynamics of H<sub>2</sub> reacting on the Cu(211) surface. A large number of TDWP calculations have been performed for all important individual rovibrational states reasonably populated in a molecular beam experiment. Our main conclusion is that the reaction of H<sub>2</sub> (D<sub>2</sub>) with Cu(211) is well described classically. This is especially true when simulating molecular beam experiments where one averages over a large number of rovibrational states and molecular beam energy distributions.

We have however found that the extent to which the reaction depends on the alignment of H<sub>2</sub> is somewhat dependent on whether QD or the QCT method is used, requiring careful validation of the dynamical model depending on the type of experiment that is being simulated. The QD method predicts stronger alignment effects on the reactivity than the QCT method for low-lying rotational states.

A comparison to recent associative desorption experiments suggest and BOMD calculations appear to show that the effect of surface atom motion and ehp's on the reactivity falls within chemical accuracy, even for the high surface temperature used in the associative desorption experiments. We saw no evidence in our fully state-resolved data for the recently reported "slow" reaction channel, even though we carried out calculations over a translational energy range where this reported reactivity should be manifested. We speculate that the "slow" reaction channel is related to surface atom motion and its modeling requires the description of this motion, which is why we did not see it here.

In contrast to the theoretical and experimental results for D<sub>2</sub> reacting on Cu(111) and Cu(100), at low translational energy, we observe a sharp downturn of the rotational quadrupole alignment parameters for vibrationally excited molecules. This downturn can be attributed to a site-specific reaction mechanism of inelastic rotational enhancement.

## AUTHOR INFORMATION

## Corresponding Author

\*E-mail: g.j.kroes@chem.leidenuniv.nl

## ORCID

Egidius W. F. Smeets: 0000-0003-0111-087X

Gernot Fuchs: 0000-0001-6062-5254

Geert-Jan Kroes: 0000-0002-4913-4689

## Notes

The authors declare no competing financial interest.

## ACKNOWLEDGMENTS

This work was supported financially by the European Research Council through an ERC-2013 advanced grant (no. 338580) and with computer time granted by NWO-EW.

## REFERENCES

- (1) Wolcott, C. A.; Medford, A. J.; Studt, F.; Campbell, C. T. Degree of rate control approach to computational catalyst screening. *J. Catal.* **2015**, *330*, 197–207.
- (2) Sabbe, M. K.; Reyniers, M.-F.; Reuter, K. First-principles kinetic modeling in heterogeneous catalysis: an industrial perspective on best-practice, gaps and needs. *Catal. Sci. Technol.* **2012**, *2*, 2010–2024.
- (3) Ertl, G. Reactions at surfaces: from atoms to complexity (Nobel lecture). *Angew. Chem., Int. Ed.* **2008**, *47*, 3524–3535.
- (4) Waugh, K. C. Methanol synthesis. *Catal. Today* **1992**, *15*, 51–75.
- (5) Grabow, L. C.; Mavrikakis, M. Mechanism of methanol synthesis on Cu through CO<sub>2</sub> and CO hydrogenation. *ACS Catal.* **2011**, *1*, 365–384.
- (6) Behrens, M.; Studt, F.; Kasatkin, I.; Köhl, S.; Hävecker, M.; Abild-Pedersen, F.; Zander, S.; Girsdsies, F.; Kurr, P.; Knief, B.-L.; et al. The active site of methanol synthesis over Cu/ZnO/Al<sub>2</sub>O<sub>3</sub> industrial catalysts. *Science* **2012**, *336*, 893–897.
- (7) Zambelli, T.; Wintterlin, J.; Trost, J.; Ertl, G. Identification of the “active sites” of a surface-catalyzed reaction. *Science* **1996**, *273*, 1688–1690.
- (8) Somorjai, G. A.; Joyner, R. W.; Lang, B. The reactivity of low index [(111) and (100)] and stepped platinum single crystal surfaces. *Proc. Royal Soc. Lond. A* **1972**, *331*, 335–346.
- (9) Kroes, G.-J. Toward a database of chemically accurate barrier heights for reactions of molecules with metal surfaces. *J. Phys. Chem. Lett.* **2015**, *6*, 4106–4114.
- (10) Polanyi, J. C. Some concepts in reaction dynamics. *Science* **1987**, *236*, 680–690.
- (11) Polanyi, J. C. Some concepts in reaction dynamics (Nobel lecture). *Angew. Chem.* **1987**, *26*, 952–971.
- (12) Slijvančanin, Ž.; Hammer, B. H<sub>2</sub> dissociation at defected Cu: preference for reaction at vacancy and kink sites. *Phys. Rev. B* **2002**, *65*, No. 085414.
- (13) Anger, G.; Winkler, A.; Rendulic, K. D. Adsorption and desorption kinetics in the systems H<sub>2</sub>/Cu(111), H<sub>2</sub>/Cu(110) and H<sub>2</sub>/Cu(100). *Surf. Sci.* **1989**, *220*, 1–17.
- (14) Berger, H. F.; Leisch, M.; Winkler, A.; Rendulic, K. D. A search for vibrational contributions to the activated adsorption of H<sub>2</sub> on copper. *Chem. Phys. Lett.* **1990**, *175*, 425–428.
- (15) Michelsen, H. A.; Rettner, C. T.; Auerbach, D. J.; Zare, R. N. Effect of rotation on the translational and vibrational energy dependence of the dissociative adsorption of D<sub>2</sub> on Cu(111). *J. Chem. Phys.* **1993**, *98*, 8294–8307.
- (16) Hou, H.; Gulding, S. J.; Rettner, C. T.; Wodtke, A. M.; Auerbach, D. J. The stereodynamics of a gas-surface reaction. *Science* **1997**, *277*, 80–82.
- (17) Comsa, G.; David, R. The purely fast distribution of H<sub>2</sub> and D<sub>2</sub> molecules desorbing from Cu(100) and Cu(111) surfaces. *Surf. Sci.* **1982**, *117*, 77–84.
- (18) Rettner, C. T.; Michelsen, H. A.; Auerbach, D. J. Quantum-state-specific dynamics of the dissociative adsorption and associative desorption of H<sub>2</sub> at a Cu(111) surface. *J. Chem. Phys.* **1995**, *102*, 4625–4641.
- (19) Rettner, C. T.; Michelsen, H. A.; Auerbach, D. J. Determination of quantum-state-specific gas–surface energy transfer and adsorption probabilities as a function of kinetic energy. *Chem. Phys.* **1993**, *175*, 157–169.
- (20) Gostein, M.; Parhikhteh, H.; Sitz, G. O. Survival probability of H<sub>2</sub> ( $v=1, J=1$ ) Scattered from Cu(110). *Phys. Rev. Lett.* **1995**, *75*, 342.
- (21) Hodgson, A.; Samson, P.; Wight, A.; Cottrell, C. Rotational excitation and vibrational relaxation of H<sub>2</sub> ( $v=1, J=0$ ) Scattered from Cu(111). *Phys. Rev. Lett.* **1997**, *78*, 963.
- (22) Watts, E.; Sitz, G. O. State-to-state scattering in a reactive system: H<sub>2</sub> ( $v=1, j=1$ ) from Cu(100). *J. Chem. Phys.* **2001**, *114*, 4171–4179.
- (23) Rettner, C. T.; Auerbach, D. J.; Michelsen, H. A. Dynamical studies of the interaction of D<sub>2</sub> with a Cu(111) surface. *J. Vac. Sci. Technol., A* **1992**, *10*, 2282–2286.
- (24) Michelsen, H. A.; Rettner, C. T.; Auerbach, D. J. On the influence of surface temperature on adsorption and desorption in the D<sub>2</sub>/Cu(111) system. *Surf. Sci.* **1992**, *272*, 65–72.
- (25) Spiering, P.; Meyer, J. Testing electronic friction models: vibrational de-excitation in scattering of H<sub>2</sub> and D<sub>2</sub> from Cu(111). *J. Phys. Chem. Lett.* **2018**, *9*, 1803–1808.
- (26) Spiering, P.; Wijzenbroek, M.; Somers, M. F. An improved static corrugation model. *J. Chem. Phys.* **2018**, *149*, 234702.
- (27) Kroes, G. J.; Wiesenekker, G.; Baerends, E. J.; Mowrey, R. C. Competition between vibrational excitation and dissociation in collisions of H<sub>2</sub> with Cu(100). *Phys. Rev. B* **1996**, *53*, 10397.
- (28) Kroes, G.-J.; Juaristi, J. I.; Alducin, M. Vibrational excitation of H<sub>2</sub> Scattering from Cu(111): effects of surface temperature and of allowing energy exchange with the surface. *J. Phys. Chem. C* **2017**, *121*, 13617–13633.
- (29) Salin, A. Theoretical study of hydrogen dissociative adsorption on the Cu(110) surface. *J. Chem. Phys.* **2006**, *124*, 104704.
- (30) Sementa, L.; Wijzenbroek, M.; van Kolck, B. J.; Somers, M. F.; Al-Halabi, A.; Busnengo, H. F.; Olsen, R. A.; Kroes, G.-J.; Rutkowski, M.; Thewes, C.; et al. Reactive scattering of H<sub>2</sub> from Cu(100): comparison of dynamics calculations based on the specific reaction parameter approach to density functional theory with experiment. *J. Chem. Phys.* **2013**, *138*, No. 044708.
- (31) Somers, M. F.; McCormack, D. A.; Kroes, G.-J.; Olsen, R. A.; Baerends, E. J.; Mowrey, R. C. Signatures of site-specific reaction of H<sub>2</sub> on Cu(100). *J. Chem. Phys.* **2002**, *117*, 6673–6687.
- (32) Nattino, F.; Diaz, C.; Jackson, B.; Kroes, G.-J. Effect of surface motion on the rotational quadrupole alignment parameter of D<sub>2</sub> reacting on Cu(111). *Phys. Rev. Lett.* **2012**, *108*, 236104.
- (33) Kroes, G.-J.; Díaz, C. Quantum and classical dynamics of reactive scattering of H<sub>2</sub> from metal surfaces. *Chem. Soc. Rev.* **2016**, *45*, 3658–3700.
- (34) Díaz, C.; Olsen, R. A.; Auerbach, D. J.; Kroes, G.-J. Six-dimensional dynamics study of reactive and non reactive scattering of H<sub>2</sub> from Cu(111) using a chemically accurate potential energy surface. *Phys. Chem. Chem. Phys.* **2010**, *12*, 6499–6519.
- (35) Díaz, C.; Pijper, E.; Olsen, R. A.; Busnengo, H. F.; Auerbach, D. J.; Kroes, G.-J. Chemically accurate simulation of a prototypical surface reaction: H<sub>2</sub> dissociation on Cu(111). *Science* **2009**, *326*, 832–834.
- (36) Wijzenbroek, M.; Somers, M. F. Static surface temperature effects on the dissociation of H<sub>2</sub> and D<sub>2</sub> on Cu(111). *J. Chem. Phys.* **2012**, *137*, No. 054703.
- (37) McCormack, D. A.; Kroes, G.-J.; Olsen, R. A.; Groeneveld, J. A.; van Stralen, J. N. P.; Baerends, E. J.; Mowrey, R. C. Quantum dynamics of the dissociation of H<sub>2</sub> on Cu(100): dependence of the site-reactivity on initial rovibrational state. *Faraday Discuss.* **2000**, *117*, 109–132.
- (38) McCormack, D. A.; Kroes, G.-J.; Olsen, R. A.; Groeneveld, J. A.; van Stralen, J. N. P.; Baerends, E. J.; Mowrey, R. C. Molecular

knife throwing: aiming for dissociation at specific surface sites through state-selection. *Chem. Phys. Lett.* **2000**, *328*, 317–324.

(39) Chen, J.; Zhou, X.; Jiang, B. Eley Rideal recombination of hydrogen atoms on Cu(111): quantitative role of electronic excitation in cross sections and product distributions. *J. Chem. Phys.* **2019**, *150*, No. 061101.

(40) Darling, G. R.; Holloway, S. Rotational motion and the dissociation of H<sub>2</sub> on Cu(111). *J. Chem. Phys.* **1994**, *101*, 3268–3281.

(41) Nienhaus, H.; Bergh, H. S.; Gergen, B.; Majumdar, A.; Weinberg, W. H.; McFarland, E. W. Electron-hole pair creation at Ag and Cu surfaces by adsorption of atomic hydrogen and deuterium. *Phys. Rev. Lett.* **1999**, *82*, 446.

(42) Sakong, S.; Groß, A. Dissociative adsorption of hydrogen on strained Cu surfaces. *Surf. Sci.* **2003**, *525*, 107–118.

(43) Kroes, G.-J.; Pijper, E.; Salin, A. Dissociative chemisorption of H<sub>2</sub> on the Cu(110) surface: A quantum and quasiclassical dynamical study. *J. Chem. Phys.* **2007**, *127*, 164722.

(44) Cao, K.; Füchsel, G.; Kleyn, A. W.; Juurlink, L. B. F. Hydrogen adsorption and desorption from Cu(111) and Cu(211). *Phys. Chem. Chem. Phys.* **2018**, *20*, 22477–22488.

(45) Kaufmann, S.; Shuai, Q.; Auerbach, D. J.; Schwarzer, D.; Wodtke, A. M. Associative desorption of hydrogen isotopologues from copper surfaces: characterization of two reaction mechanisms. *J. Chem. Phys.* **2018**, *148*, 194703.

(46) Füchsel, G.; Cao, K.; Er, S.; Smeets, E. W. F.; Kleyn, A. W.; Juurlink, L. B. F.; Kroes, G.-J. Anomalous dependence of the reactivity on the presence of steps: dissociation of D<sub>2</sub> on Cu(211). *J. Phys. Chem. Lett.* **2017**, *9*, 170–175.

(47) Ghassemi, E. N.; Smeets, E. W. F.; Somers, M. F.; Kroes, G.-J.; Groot, I. M. N.; Juurlink, L. B. F.; Füchsel, G. Transferability of the specific reaction parameter density functional for H<sub>2</sub> + Pt(111) to H<sub>2</sub> + Pt(211). *J. Phys. Chem. C* **2019**, *123*, 2973–2986.

(48) Olsen, R. A.; McCormack, D. A.; Baerends, E. J. How molecular trapping enhances the reactivity of rough surfaces. *Surf. Sci.* **2004**, *571*, L325–L330.

(49) McCormack, D. A.; Olsen, R. A.; Baerends, E. J. Mechanisms of H<sub>2</sub> dissociative adsorption on the Pt(211) stepped surface. *J. Chem. Phys.* **2005**, *122*, 194708.

(50) Luppi, M.; McCormack, D. A.; Olsen, R. A.; Baerends, E. J. Rotational effects in the dissociative adsorption of H<sub>2</sub> on the Pt(211) stepped surface. *J. Chem. Phys.* **2005**, *123*, 164702.

(51) Olsen, R. A.; McCormack, D. A.; Luppi, M.; Baerends, E. J. Six-dimensional quantum dynamics of H<sub>2</sub> dissociative adsorption on the Pt(211) stepped surface. *J. Chem. Phys.* **2008**, *128*, 194715.

(52) Huang, X.; Yan, X. H.; Xiao, Y. Effects of vacancy and step on dissociative dynamics of H<sub>2</sub> on Pd(111) surfaces. *Chem. Phys. Lett.* **2012**, *531*, 143–148.

(53) Hammer, B.; Nørskov, J. K. Electronic factors determining the reactivity of metal surfaces. *Surf. Sci.* **1995**, *343*, 211–220.

(54) Hammer, B.; Nørskov, J. K. Why gold is the noblest of all the metals. *Nature* **1995**, *376*, 238.

(55) Mavrikakis, M.; Hammer, B.; Nørskov, J. K. Effect of strain on the reactivity of metal surfaces. *Phys. Rev. Lett.* **1998**, *81*, 2819.

(56) Pijper, E.; Kroes, G.-J.; Olsen, R. A.; Baerends, E. J. Reactive and diffractive scattering of H<sub>2</sub> from Pt(111) studied using a six-dimensional wave packet method. *J. Chem. Phys.* **2002**, *117*, 5885–5898.

(57) Kroes, G.-J.; Somers, M. F. Six-dimensional dynamics of dissociative chemisorption of H<sub>2</sub> on metal surfaces. *J. Theor. Comput. Chem.* **2011**, *04*, 493–581.

(58) Wijzenbroek, M.; Klein, D. M.; Smits, B.; Somers, M. F.; Kroes, G.-J. Performance of a non-local van der Waals density functional on the dissociation of H<sub>2</sub> on metal surfaces. *J. Phys. Chem. A* **2015**, *119*, 12146–12158.

(59) Busnengo, H. F.; Salin, A.; Dong, W. Representation of the 6D potential energy surface for a diatomic molecule near a solid surface. *J. Chem. Phys.* **2000**, *112*, 7641–7651.

(60) Wei, C. Y.; Lewis, S. P.; Mele, E. J.; Rappe, A. M. Structure and vibrations of the vicinal copper (211) surface. *Phys. Rev. B* **1998**, *57*, 10062–10068.

(61) Hammer, B.; Hansen, L. B.; Nørskov, J. K. Improved adsorption energetics within density-functional theory using revised Perdew-Burke-Ernzerhof functionals. *Phys. Rev. B* **1999**, *59*, 7413–7421.

(62) Perdew, J. P.; Burke, K.; Ernzerhof, M. Generalized gradient approximation made simple. *Phys. Rev. Lett.* **1996**, *77*, 3865–3868.

(63) Kresse, G.; Hafner, J. Ab initio molecular-dynamics simulation of the liquid-metal–amorphous-semiconductor transition in germanium. *Phys. Rev. B* **1994**, *49*, 14251–14269.

(64) Kresse, G.; Hafner, J. Ab initio molecular dynamics for liquid metals. *Phys. Rev. B* **1993**, *47*, 558–561.

(65) Kresse, G.; Furthmüller, J. Efficient iterative schemes for ab initio total-energy calculations using a plane-wave basis set. *Phys. Rev. B* **1996**, *54*, 11169–11186.

(66) Kresse, G.; Furthmüller, J. Efficiency of ab-initio total energy calculations for metals and semiconductors using a plane-wave basis set. *Comput. Mater. Sci.* **1996**, *6*, 15–50.

(67) Blanco-Rey, M.; Juaristi, J. I.; Díez Muiño, R.; Busnengo, H. F.; Kroes, G.-J.; Alducin, M. Electronic friction dominates hydrogen hot-atom relaxation on Pd(100). *Phys. Rev. Lett.* **2014**, *112*, 103203.

(68) Novko, D.; Blanco-Rey, M.; Juaristi, J. I.; Alducin, M. Ab initio molecular dynamics with simultaneous electron and phonon excitations: Application to the relaxation of hot atoms and molecules on metal surfaces. *Phys. Rev. B* **2015**, *92*, 201411.

(69) Füchsel, G.; del Cueto, M.; Díaz, C.; Kroes, G.-J. Enigmatic HCl + Au(111) reaction: a puzzle for theory and experiment. *J. Phys. Chem. C* **2016**, *120*, 25760–25779.

(70) Raff, L. M.; Karplus, M. Theoretical investigations of reactive collisions in molecular beams: K+CH<sub>3</sub>I and related systems. *J. Chem. Phys.* **1966**, *44*, 1212–1229.

(71) Lemons, D. S.; Gythiel, A. Paul Langevin's 1908 paper "On the Theory of Brownian Motion" ["Sur la théorie du mouvement brownien," C. R. Acad. Sci. (Paris) *146*, 530–533 (1908)]. *Am. J. Phys.* **1997**, *65*, 1079–1081.

(72) Ermak, D. L.; Buckholz, H. Numerical integration of the Langevin equation: Monte Carlo simulation. *J. Comput. Phys.* **1980**, *35*, 169–182.

(73) Füchsel, G.; Klamroth, T.; Monturet, S.; Saalfrank, P. Dissipative dynamics within the electronic friction approach: the femtosecond laser desorption of H<sub>2</sub>/D<sub>2</sub> from Ru(0001). *Phys. Chem. Chem. Phys.* **2011**, *13*, 8659–8670.

(74) Juaristi, J. I.; Alducin, M.; Díez Muiño, R.; Busnengo, H. F.; Salin, A. Role of electron-hole pair excitations in the dissociative adsorption of diatomic molecules on metal surfaces. *Phys. Rev. Lett.* **2008**, *100*, 116102.

(75) Vibok, A.; Balint-Kurti, G. G. Parametrization of complex absorbing potentials for time-dependent quantum dynamics. *J. Phys. Chem.* **1992**, *96*, 8712–8719.

(76) Balint-Kurti, G. G.; Dixon, R. N.; Marston, C. C. Grid methods for solving the Schrödinger equation and time dependent quantum dynamics of molecular photofragmentation and reactive scattering processes. *Int. Rev. Phys. Chem.* **1992**, *11*, 317–344.

(77) Michelsen, H. A.; Auerbach, D. J. A critical examination of data on the dissociative adsorption and associative desorption of hydrogen at copper surfaces. *J. Chem. Phys.* **1991**, *94*, 7502–7520.

(78) Zare, R. N.; Harter, W. G. Angular momentum: understanding spatial aspects in chemistry and physics. *Phys. Today* **1989**, *42*, 68.

(79) Shakouri, K.; Behler, J.; Meyer, J.; Kroes, G.-J. Accurate neural network description of surface phonons in reactive gas-surface dynamics: N<sub>2</sub>+ Ru(0001). *J. Phys. Chem. Lett.* **2017**, *8*, 2131–2136.

(80) Díaz, C.; Perrier, A.; Kroes, G.-J. Associative desorption of N<sub>2</sub> from Ru(0001): a computational study. *Chem. Phys. Lett.* **2007**, *434*, 231–236.

(81) Muzas, A. S.; Juaristi, J. I.; Alducin, M.; Díez Muiño, R.; Kroes, G.-J.; Díaz, C. Vibrational deexcitation and rotational excitation of H<sub>2</sub>

and D<sub>2</sub> scattered from Cu(111): adiabatic versus non-adiabatic dynamics. *J. Chem. Phys.* **2012**, *137*, No. 064707.